

Fabrication and characterization of a magnetic biocomposite of magnetite nanoparticles and reduced graphene oxide for biomedical applications

Yulia R. Mukhortova^a, Artyom S. Pryadko^a, Roman V. Chernozem^a, Igor O. Pariy^a,
 Elizaveta A. Akoulina^b, Irina V. Demianova^b, Irina I. Zharkova^b, Yuri F. Ivanov^c,
 Dmitriy V. Wagner^d, Anton P. Bonartsev^b, Roman A. Surmenev^a, Maria A. Surmeneva^{a,*}

^a Physical Materials Science and Composite Materials Centre, Research School of Chemistry & Applied Biomedical Sciences, National Research Tomsk Polytechnic University, 634050, Tomsk, Russia

^b Faculty of Biology, M.V. Lomonosov Moscow State University, Leninskie Gory 1-12, 119234 Moscow, Russia

^c Institute of High Current Electronics (IHCE), 2/3 Akademicheskoy Avenue, 634055, Tomsk, Russia

^d National Research Tomsk State University, 634050, Tomsk, Russia

ARTICLE INFO

Article history:

Received 31 October 2021

Received in revised form 23 December 2021

Accepted 25 January 2022

Keywords:

Magnetite nanoparticles

Reduced graphene oxide

Composite

Biomedical applications

Saturation magnetization

ABSTRACT

Functionalization of magnetite (Fe_3O_4) nanoparticles with reduced graphene oxide (rGO) with the preserved magnetic properties of the former presents great potential for applying the $\text{Fe}_3\text{O}_4/\text{rGO}$ biocomposite in various biomedical applications, such as magnetic resonance imaging, as a therapeutic component in initiating tumour cell death in magnetic and photon ablation therapy, and as an effective carrier for drug delivery. In this study, magnetite nanoparticles (MNPs) with a high saturation magnetization were synthesized by co-precipitation under various conditions, followed by covalent functionalization with citric acid (CA) and subsequent attachment to rGO sheets by physical adsorption. Extensive characterization revealed increasing phase purity with a subsequent decrease in the crystallite size and average size of the MNPs synthesized in an inert atmosphere compared to ambient conditions. Meanwhile, further functionalization of the MNPs with CA by covalent binding does not affect the MNP structure and size, but decreases their agglomeration. To study the magnetic properties of the MNPs and the $\text{Fe}_3\text{O}_4/\text{rGO}$ composite, magnetization curves were obtained with a vibrating sample magnetometer at a pulsed magnetic field of up to 6.5 kOe. The largest values of saturation magnetization are revealed for the samples synthesized without the addition of CA in an inert atmosphere ($\sigma_s = 80.27 \text{ emu/g}$). The addition of CA to the synthesized MNPs and $\text{Fe}_3\text{O}_4/\text{rGO}$ composites reduced agglomeration, with σ_s values in the range from 64.10 to 60.97 emu/g. *In vitro* biological experiments revealed the MNP concentrations that did not cause any toxic effects on cells for use as magnetic fillers to investigate the strain-mediated effects of hybrid polymer composites on cellular behaviour due to external magnetic field exposure in the next stages of research.

© 2022 Elsevier B.V. All rights reserved.

1. Introduction

There is great interest in superparamagnetic nanoparticles (NPs) due to their potential application in biomedicine. They can be used to enhance contrast in magnetic resonance imaging (MRI) for molecular and cell imaging [1]. Magnetite (Fe_3O_4) NPs (MNPs) exhibit strong relaxation properties, significantly larger than those of paramagnetic molecules used as MRI contrast agents, e.g. Gd-chelates [2]. Magnetic resonance (MR) contrast generation with MNPs is influenced by their size, structure and

the presence of trace phases [3]. It has been reported that an increase in the MNP size results in improved MR contrast [4]. MNPs can be functionalized with different drugs and used as magnetic field-guided drug delivery agents [5]. MNPs exposed to an alternating magnetic field can generate heat by energy dissipation to achieve an intracellular hyperthermia effect [6,7]. Thus, the combination of anticancer drugs and hyperthermic effects makes MNPs very attractive for cancer therapy [8,9].

There are also reports of using MNPs for metal ion removal from aqueous solutions [10] and cell separation [11]. The particle size [12], shape [13], size distribution [14] and magnetic properties [15] strongly depend on the synthesis route. There are various methods of MNP fabrication, but thermal decomposition and co-precipitation are the most commonly used [16]. The thermal

* Corresponding author.

E-mail address: surmenevmaria@mail.ru (M.A. Surmeneva).

decomposition method allows for the production of high-quality superparamagnetic MNPs, but the organic precursors of iron, such as $\text{Fe}(\text{CO})_5$ and $\text{Fe}(\text{acac})_3$ (iron acetylacetonate), involved in this method are toxic and may cause a negative cellular response [17]. In turn, the chemical co-precipitation method allows the preparation of MNPs with a spherical shape and size below 25 nm with a homogeneous size distribution [18].

However, MNPs tend to form aggregates due to their magnetic properties and long-range van der Waals interactions [19]. MNPs can agglomerate due to strong anisotropic dipolar interactions, which severely affect their properties [19]. To prevent agglomeration, MNPs are synthesized via surface modification with other compounds or coated with an active surface layer [20]. Fe_3O_4 NP aggregation can also take place before functionalization with rGO. In this regard, the functionalization of MNPs with oleic and citric acids (CA) helps to prevent agglomeration and enhance the resistance against magnetite oxidation into maghemite, thereby providing a more uniform distribution of the NPs' shape and size as well as phase purity and as a consequence the magnetic properties [17,21,22].

As an alternative, graphene derivatives, such as reduced graphene oxide (rGO), have a high specific surface area, mechanical strength and biocompatibility [23]. rGO has been investigated for drug delivery of water insoluble aromatic anticancer drugs into cells [24] as well as for their antibacterial effects [25,26]. In the case of rGO, sheet defects, poor dispersion, restacking and multilayer thickness significantly limit the utilization of the 2D materials' high surface area and properties [23]. To make full use of the unique properties of 2D materials, it is necessary to isolate them from the bulk in several layers, or even in one layer, using mechanical or liquid phase exfoliation processes. The liquid exfoliation method by mechanical sonication is an effective way to disperse 2D materials, but the dispersion is sometimes unstable and tends to reaggregate [24].

It has been reported that during the synthesis of $\text{Fe}_3\text{O}_4/\text{rGO}$ composites, rGO nanosheets can prevent the aggregation of Fe_3O_4 microspheres; at the same time, the Fe_3O_4 microspheres can improve the aggregation stability of the rGO nanosheets [27,28]. Functionalization of MNPs with rGO can contribute not only to a decrease in their agglomeration but also to an increase in their electrical conductivity while maintaining their magnetic properties [29]. In addition, in case of the composite of $\text{Fe}_3\text{O}_4/\text{rGO}$, even at a small rGO content, one can expect an increase of the specific surface area of the composite compared with pure Fe_3O_4 (13.1 m^2/g) [30], and as a consequence an increase of the efficiency and adsorption rate of drugs and/or other bioactive compounds, whilst keeping the magnetic properties high [31].

Composites of $\text{Fe}_3\text{O}_4/\text{rGO}$ are reported to be used in various biomedical applications. For example, a high content of Fe_3O_4 in the nanocomposite was effective for improving both the osteoconductivity and heat generation characteristics for hyperthermia applications [30]. The composite of $\text{Fe}_3\text{O}_4/\text{rGO}$ has also been applied for the removal of toxic elements and compounds from contaminated water, including the sorption of antibiotics. Such a composite responds to a magnet, which could realize the retrieval and separation of rGO rapidly and effectively [25]. A number of developments have been devoted to the use of composites in the areas of drug loading [31], separation and chemical extraction [32], sensors and biosensors due to the synergistic effect between the rGO matrix and Fe_3O_4 , which aims to increase conductivity and ionic diffusion, leading to a material with superior electrochemical performance [33]. Hence, $\text{Fe}_3\text{O}_4/\text{rGO}$ composites have various prospective applications due to the combination of the magnetic properties of Fe_3O_4 and rGO, namely, high conductivity, large surface-to-volume ratio, high magnetization values and the possibility of being controlled using an external magnetic field [32].

Despite many works being devoted to the biomedical applications of $\text{Fe}_3\text{O}_4/\text{rGO}$ composites, the actual mechanism of interaction between these phases has not been sufficiently studied to the best of our knowledge, which makes fabrication of the composite with tailored properties for biomedical applications quite challenging [33]. In addition, it is reported that rGO induced cytotoxicity, apoptosis and oxidative stress, therefore, the fabrication of biocompatible composite materials which hallow overcoming this significant drawback is required; as a prospective example the $\text{Fe}_3\text{O}_4/\text{rGO}$ composite can be prepared [33]. Thus, the present study is aimed at the revealing of the most appropriate routes to prepare nanometre-size MNPs with the highest saturation magnetization, namely, the change in the synthesis atmosphere and the use of citrate ions to prevent particle agglomeration before functionalization with rGO. It is envisaged that the $\text{Fe}_3\text{O}_4/\text{rGO}$ composites will provide high values of saturation magnetization, increased specific surface area for efficient drug loading capacity, better electrical conductivity and biocompatibility compared to either the pure MNPs or rGO.

2. Materials and methods

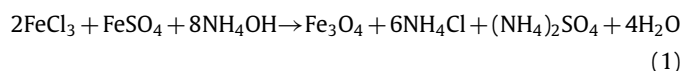
2.1. Precursors

The reagents used in the experiments were as follows: hydrochloric acid (HCl), sodium hydroxide (NaOH), ferric(III) chloride hexahydrate ($\text{FeCl}_3 \cdot 6\text{H}_2\text{O}$), ferric(II) sulphate heptahydrate ($\text{FeSO}_4 \cdot 7\text{H}_2\text{O}$), ammonium hydroxide (NH_4OH), CA ($\text{C}_6\text{H}_8\text{O}_7$) and rGO, which were purchased from Sigma-Aldrich. De-ionized water was also used in the experiments.

2.2. $\text{Fe}_3\text{O}_4/\text{rGO}$ composites preparation

2.2.1. Synthesis of MNPs

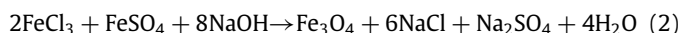
The Fe_3O_4 NPs were synthesized by a co-precipitation method using two different methodologies. Prior to the first synthesis of Fe_3O_4 MNPs at room temperature, the pH of the solution was adjusted to 2 using HCl to avoid the formation of iron oxide impurities other than magnetite [34]. It should be noted that the $\text{Fe}^{2+}:\text{Fe}^{3+}$ ratio in $\text{mFe}_2\text{O}_3 \cdot \text{nFeO}$ precipitation results in high purity Fe_3O_4 precipitation when $\text{m} = \text{n}$ (equimolar ratio) [35]. When m and n are not equal, excess Fe^{3+} or Fe^{2+} ions will precipitate as iron oxides, FeO or Fe_3O_4 , respectively. However, the impurities in FeO disturb the structure of Fe_3O_4 , and the magnetization of the mixture of FeO and Fe_3O_4 is lower than that of pure Fe_3O_4 . These two factors lead to a decrease in the saturation magnetization. Theoretically, the $\text{Fe}^{3+}:\text{Fe}^{2+}$ molar ratio should be 2, but in the case where no inert gas was used and the solution had direct contact with air, Fe^{2+} was easily oxidized to Fe^{3+} under these conditions. In addition, under the conditions where Fe^{2+} was easily oxidized, $\alpha\text{-FeOOH}$ was formed under alkaline conditions, which reduces the purity of the product. Therefore, we used excess Fe^{2+} to compensate for this deficiency [35]. In the present study, the $\text{Fe}^{3+}/\text{Fe}^{2+}$ molar ratio was always 1.5. The MNPs were obtained according to the following reaction (1):



For this synthesis, 2.80 g of ferric(III) chloride hexahydrate and 1.92 g of ferric(II) sulphate heptahydrate were placed in a three-necked flask, dissolved in 25 mL of deionized water and stirred with a magnetic stirrer for 1 h at 300 rpm without heating. Then, a few drops of HCl were added to the solution to give a pH value of 1–2, followed by heating at 85 °C for 45 min. Then, the solution was cooled to room temperature. In the next

step, the rotation speed was increased to 1500 rpm and 8 mL of concentrated NH_4OH was added dropwise until pH 11 was reached, while a colour change from light orange to black was observed, indicating the formation of magnetite particles. After that, the reaction mass was stirred for 60 min. The resulting solution was washed with deionized water. The particles were separated by magnetic separation and dried at 35 °C for two days in a convection oven. To examine the influence of the atmosphere in the reaction zone on the morphology and crystallinity of the products, the Fe_3O_4 NPs were also synthesized in ambient and nitrogen atmospheres while keeping the other conditions unchanged. An inert atmosphere allows the exclusion of oxygen from the atmosphere, which participates in the formation of non-magnetic oxide impurities [36].

The second synthesis of MNPs, with heating up to 60 °C, can be described by the following reaction (2) [37]:



To perform the synthesis, 3.73 g of ferric(III) chloride hexahydrate and 1.92 g of ferric(II) sulphate heptahydrate were loaded into a three-necked flask, which was placed on a magnetic stirrer and connected to the Schlenk system. Dry salts were alternately degassed using a vacuum unit and saturated with argon three times. Then, using a syringe, 175 mL of deionized water was introduced into the flask, followed by stirring and heating on a magnetic stirrer. The solution was heated to a temperature of 60 °C with stirring at a speed of 300 rpm for 30 min. The removal of oxygen was achieved by passing argon through the reaction mixture throughout the entire synthesis. Upon reaching the specified temperature, the stirring speed was increased to 1500 rpm, and 50 mL of 1.5 M NaOH heated to 60 °C was added to the solution dropwise with a syringe to shift the pH level to 11. At the same time, blackening of the solution was observed, which indicates the formation of magnetite. Heating was continued for 30 min.

To reduce or eliminate the aggregation of MNPs, after 30 min of continuous heating, 3.7 mL of CA (0.5 g in 1 mL of water) was introduced into the solution, and the temperature was increased to 80 °C with continuous stirring for 90 min. After completion of the synthesis, the solution was decanted and the powders were washed with deionized water. The washing procedure was repeated until neutral pH was reached and then the powders were precipitated by an external magnetic field and dried at 35 °C in a convection oven for two days. As a result, black magnetite powders were obtained. To study the effect of CA on the morphology and parameters of the Fe_3O_4 NPs, the materials were obtained without and with CA treatment while keeping the other conditions unchanged.

2.2.2. Synthesis of the composite of $\text{Fe}_3\text{O}_4/\text{rGO}$

Prior to the $\text{Fe}_3\text{O}_4/\text{rGO}$ composite preparation, the surface of rGO was prepared by the impregnation method before synthesis, in which a solution of 0.1 g of rGO in 8 mL of 0.25 M NaOH was placed in an ultrasonic bath for 4 h and then heated on a magnetic stirrer for 20 h at 60 °C. Soaking of rGO in an alkaline solution causes electrostatic repulsion of negatively charged layers and leads to exfoliation and thereby dispersion stabilization of rGO [38], which is necessary for further uniform distribution of magnetite nanoparticles on the rGO sheets.

For the synthesis of the $\text{Fe}_3\text{O}_4/\text{rGO}$ composite, as-prepared MNPs and rGO sheets were used. The synthesis of the $\text{Fe}_3\text{O}_4/\text{rGO}$ composite was performed by mixing magnetite and rGO at room temperature with slow magnetic stirring at 160 rpm. The processing time to obtain a composite sample was 2 h. Then, the reaction mass was infused for 2 h without stirring. After thorough mixing of Fe_3O_4 and rGO, the final mixture was washed with deionized

Table 1

Description of the prepared samples and synthesis details.

Composite	MNPs synthesis atmosphere	Abbreviations	Ratio ($\text{Fe}_3\text{O}_4/\text{rGO}$)
Fe_3O_4	Air	M1	–
Fe_3O_4	Nitrogen	M1N	–
Fe_3O_4	Argon	M2	–
Fe_3O_4	Argon with CA	M2CA	–
$\text{Fe}_3\text{O}_4/\text{rGO}$	Nitrogen	M1N/rGO	6:1
$\text{Fe}_3\text{O}_4/\text{rGO}$	Argon with CA	M2CA/rGO	6:1

water and the composite obtained was precipitated via magnetic separation, thus any unreacted rGO was removed. The resulting precipitate was dried at 35 °C for two days in a convection oven. Thus, only MNPs adsorbed on the surface of rGO nanoflakes were prepared and investigated.

The abbreviations of the samples with the corresponding fabrication parameters are presented in Table 1.

2.3. Characterization of the samples

The phase composition was analysed by X-ray diffraction on a Shimadzu XRD 7000S diffractometer (CuK_α radiation) equipped with a high-speed 1280-channel OneSight detector. The study was carried out in the automatic mode with the range of scattering angles from 5 to 80°. The crystallite size (nm) was calculated according to the Scherrer Eq. (3) from the full width at half maximum of the diffraction peaks in the angular 2θ range of 30–45° [39]:

$$d = \frac{K\lambda}{\beta \cos\theta}, \quad (3)$$

where λ is X-ray wavelength (nm), β is peak width at half height (rad), K is the dimensionless particle shape factor (usually taken as being equal to 0.9) [40] and θ (°) is the diffraction angle.

Prior to the study of the morphology, a conductive coating of Au was deposited on the samples. Scanning electron microscopy (SEM) (Quanta 600 electron microscope (Thermo Fisher, Japan)) equipped with energy dispersive spectroscopic analysis (EDS) was performed to evaluate the changes in the morphology and elemental composition of the samples. The electrical conductivity of rGO highly depends on the degree of reduction and can vary in a broad range between separate nanoflakes. Moreover, in the present study, rGO was studied as a component of the composite with magnetite NPs, whereas, magnetite may also reveal semi-conducting properties. Thus, the sputtering of a thin conductive Au coating (5 nm) was experimentally adopted to improve the resolution to obtain representative SEM images. Transmission electron microscope (TEM) images and selected area electron diffraction (SAED) patterns were obtained on a Hitachi HU-11B at an accelerating voltage of 200 kV. The samples were prepared by placing a drop of the nanoparticle suspension on a carbon-coated Cu grid. The distribution of the diameters of the synthesized particles was measured using ImageJ software.

The Fourier-transform infrared (FTIR) spectra were recorded using a Tensor 27 Fourier transform IR spectrometer (Bruker, Germany). FTIR spectra were processed from 128 scans at a 4 cm^{-1} resolution in the attenuated total reflection mode for each sample.

Raman spectra were obtained using an InVia confocal dispersive Raman spectrometer (Renishaw, UK) equipped with a Leica microscope and a 50x objective. Excitation was performed with a semiconductor laser at a wavelength of 528 nm with a maximum power of 100 mW. To prevent heating of the sample and phase transformations, 5% of the laser power was used. To attenuate the radiation, 100% beam defocusing was additionally applied.

The magnetic properties of the MNPs and $\text{Fe}_3\text{O}_4/\text{rGO}$ composites were investigated at a temperature of 300 K with an external pulsed magnetic field from 0 to 6.5 kOe using a pulsed magnetometer. The measurements were carried out according to the method described in [41].

2.4. In vitro assays

2.4.1. Materials for cell culture experiments

The culture media included Dulbecco's modified Eagle medium (DMEM) (PanEco, Russia), FBS foetal bovine serum (FBS) (Biolot, Russia), antibiotic penicillin–streptomycin (PanEco, Russia) and phosphate-buffered saline (PBS) (Merck, Germany); thiazolyl blue tetrazolium bromide (MTT reagent) (Merck, Germany) was used for cell viability testing.

2.4.2. Cell culture methods to determine the cytotoxicity

Evaluation of the $\text{Fe}_3\text{O}_4/\text{rGO}$ composite biocompatibility *in vitro* was performed on cultures of mesenchymal stem cells (MSCs) of Wistar rats; cells were isolated from the adipose tissue of 3-day-old male rats [42]. Solutions of each magnetite sample were made in growth medium (DMEM 89%, FBS 10%, penicillin–streptomycin 1%) at different concentrations. The cells were cultivated before the experiment in the same growth medium for two passages. The cells were placed in a 96-well plate at a density of 2000 per well and the medium in the wells was replaced with magnetite solutions after one day of incubation.

Stock solutions of all the fabricated particles in growth media were made with a concentration of 100 $\mu\text{g}/\text{mL}$ (20 μg in 200 μL – the volume of liquid introduced into one well). Further dilutions for each solution were made 3, 10, 30 and 100 times with concentrations of 33, 10, 3 and 1 $\mu\text{g}/\text{mL}$, respectively. Using these dilutions, a cytotoxicity test was performed. The cells were seeded in 96-well plates, and growth media was replaced in the solution with samples after 24 h of incubation. The cell viability in the presence of the synthesized NPs and composites was assessed by the MTT method on days 1 and 3 of incubation. To determine the viability, the medium with samples was removed and 50 μL of DMEM and 50 μL of MTT reagent (5 mg/mL) were placed into each well. After incubation for 3 h at 37 °C, 150 μL of DMSO was added to each well and, after incubation for 10 min, spectrophotometric data were obtained at 595 and 620 nm (as a reference absorbance). The calibration plot “cell number—absorbance at 450 nm” was built using a known number of the same cells counted by light microscopy on the micron scale. The criterion for cytotoxicity was a decrease of the cell viability below 70% of the control, according to Annex C ISO 10993-5 Tests for *in vitro* cytotoxicity.

2.5. Statistical analysis

The experiments were conducted with 3 samples for each composite material. The non-parametric Kruskal–Wallis test was employed for the statistical evaluation of data using the software package SPSS/PC+ Statistics™ 12.1 (SPSS: An IBM Company, Armonk, NY, USA). The obtained data are presented as the mean \pm SD (standard error of the mean) and were considered significant at $p < 0.05$.

3. Results and discussion

3.1. Investigation of the morphology and structure of the magnetite nanoparticles

Fig. 1 shows the SEM images and size distributions of the MNPs synthesized by various methods.

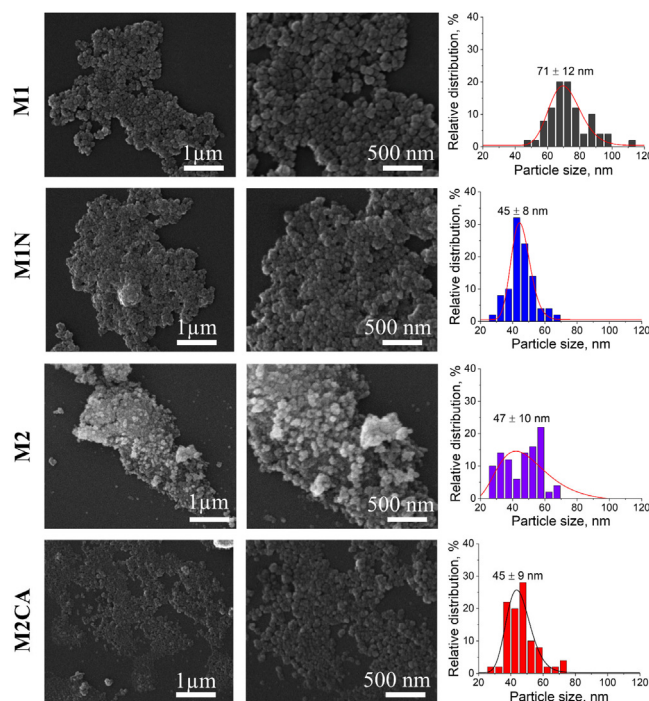


Fig. 1. SEM images of MNPs synthesized under different conditions: M1 – room temperature in air atmosphere; M1N – room temperature in an inert (N_2) atmosphere; M2 – process with heating to 60 °C in an inert (Ar) atmosphere; M2CA – process with heating to 60 °C in an inert (Ar) atmosphere and addition of CA.

The average sizes of the MNPs obtained at room temperature in air (M1) and nitrogen (M1N) atmospheres were 75 ± 12 and 46 ± 8 nm, respectively. In the case of heating in an argon atmosphere, CA-uncoated (M2) and coated (M2CA) MNPs were 46 ± 10 and 47 ± 9.3 nm, respectively. The MNPs obtained in the present study by varying the synthesis parameters (e.g., atmosphere and CA doping) had an average size from 46 ± 8 to 75 ± 12 nm, which is different from that (20–30 nm) of the particles reported elsewhere [22,37].

Notably, the diameter of the NPs did not change significantly when an inert atmosphere was used. It is known that the process of magnetite fabrication in an inert atmosphere prevents the formation of other iron oxide compounds, thereby increasing the phase purity and enhancing the magnetic properties of the final product. The effect of the inert atmosphere was also reflected by the decrease in the average particle diameter for M1N NPs compared to M1 NPs synthesized under ambient conditions. This is explained by the dense magnetite's inverse spinel crystal structure, which possesses a smaller unit cell that does not have free vacancies compared with Fe-oxide impurities on surface for M1 [43]. Maghemite, similar to haematite and goethite, is a fully oxidized iron oxide polymorph where all the iron is in the Fe^{3+} state, and the maghemite crystal structure possesses 2 and 1/3 vacant sites within its unit cell and is packed less densely [44].

Samples M1 and M1N were obtained without the use of surface-active additives, which prevented particle aggregation. As a result, dense accumulations and agglomerates of MNPs were observed in the images of samples M1, M1N and M2. In contrast, the M2CA sample, obtained using a citrate ion coating, appears to be less agglomerated. The use of a citrate ion coating also contributes to the formation of finer particles and stabilization of magnetite particles against agglomeration [45]. The adsorption properties of magnetite are due to its chemical nature and are the basis of its interaction with the CA stabilizer. The centres

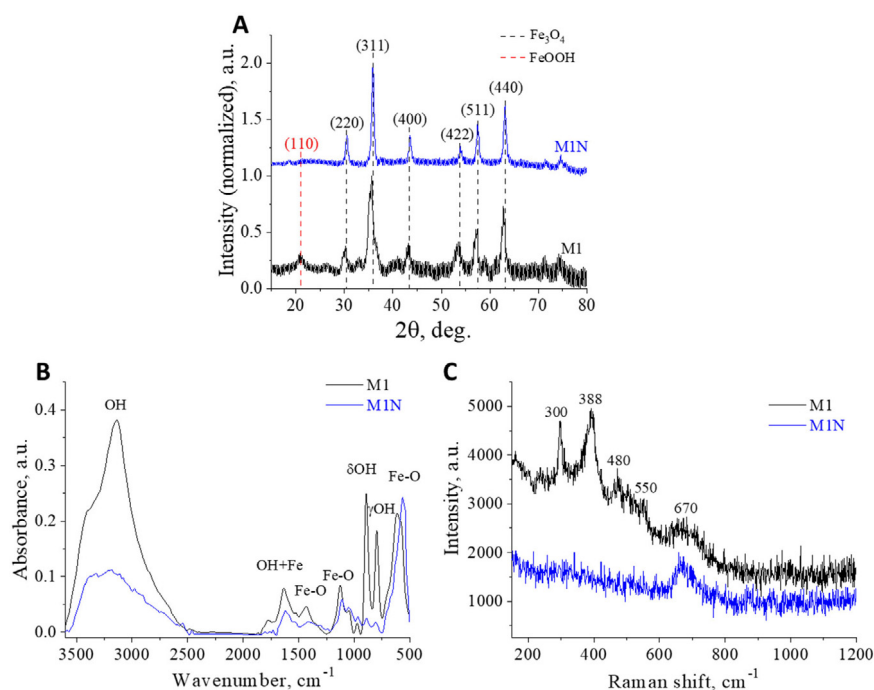


Fig. 2. (A) X-ray diffraction patterns, (B) FTIR and (C) Raman spectra of synthesized MNPs: M1 — at room temperature in an air atmosphere; M1N — at room temperature in an inert atmosphere.

of adsorption on the surface of magnetite can be coordination-unsaturated Fe³⁺ and Fe²⁺ ions, as well as ²⁻ and ⁻ ions, formed as a result of dissociative chemisorption of oxygen and water on its freshly formed surface [45]. Due to the presence of 3d-vacant and 3d-filled orbitals, the iron atoms can participate in chemical reactions as electron donors and acceptors [45].

Fig. 2 shows the results of MNPs synthesized under various experimental conditions. Fig. 2A demonstrates that the samples exhibit peaks at $2\theta = 30.35, 35.63, 43.49, 53.56, 57.12$ and 62.81° , corresponding to the d_{hkl} crystal planes of magnetite at (220), (311), (400), (422), (511) and (440), respectively. These results are in good agreement with the standard peaks of the Fe₃O₄ XRD pattern (PDF card 01-080-6403). However, sample M1 also contains a reflection corresponding to the goethite (FeOOH) phase at $2\theta = 21.22^\circ$ [46]. The quantitative analysis showed that the phase distribution of synthesized M1 was as follows: Fe₃O₄ — 64.8% and FeOOH — 35.2%. In contrast, the sample obtained in a nitrogen atmosphere (M1N) fully corresponds to the standard XRD pattern of Fe₃O₄, which shows the high purity of the prepared sample. Due to the cubic symmetry of the MNPs, the average crystallite size can be calculated by the Scherrer equation (1) from the full width at half maximum of the diffraction peaks in the angular 2θ range of $30\text{--}45^\circ$ [39]. Thus, the average crystallite sizes for M1 and M1N were $d = 40 \pm 12$ and 16 ± 5 nm, respectively. This difference can be explained by M1 being obtained under ambient conditions, thus oxygen from the air can contribute to the growth kinetics of the magnetite crystals.

FTIR spectra of the MNPs obtained in air (M1) and in a nitrogen atmosphere (M1N) are shown in Fig. 2B. Both spectra demonstrate the typical absorption bands of MNPs at $\sim 580, 1110$ and 1400 cm^{-1} , corresponding to Fe–O vibrations for magnetite [47]. However, the presence of the 1110 cm^{-1} band can also be associated with other iron oxides, such as maghemite [47]. The observed band at 1614 cm^{-1} is associated with OH bending vibrations in combination with Fe atoms [48], while the broad band at $2500\text{--}3550\text{ cm}^{-1}$ refers to the stretching vibrations of OH groups [47]. The bands at 891 cm^{-1} (δ OH in-plane bending vibrations) and 794 cm^{-1} (γ OH out-of-plane bending vibrations)

present in the spectrum of the M1 sample are attributed to Fe–OH bending vibrations of the non-magnetic phase of the iron oxide, goethite [49]. Moreover, the Fe–O band at 580 cm^{-1} shifted to $\sim 620\text{ cm}^{-1}$, indicating the presence of a goethite phase in the M1 sample [50]. In addition, the Raman spectrum of MNPs obtained in air (M1) exhibited characteristic peaks of the goethite phase (Fig. 2C), as follows: at 300 cm^{-1} (Fe–OH symmetric bending vibrations), at 388 cm^{-1} (Fe–O–Fe/OH group symmetric stretching vibrations), at 480 and 550 cm^{-1} (Fe–OH asymmetric stretching vibrations) [51]. In turn, MNPs synthesized in an inert (nitrogen) atmosphere exhibited only a peak at 670 cm^{-1} associated with Fe–O symmetric stretching vibrations, which indicates the presence of a magnetite phase [52,53].

CA is a water-soluble biocompatible (Krebs cycle) surfactant that exists in the human body and is involved in the three carboxylic acid cycle (TCAC), contributing to the decomposition of fat [46,54]. It is used to control the morphology of magnetite particles [55] to achieve stability against aggregation [37]. The presence of three free carboxyl groups and one hydroxyl group in CA provides maximum chemical interaction (chemisorption) with the surface of magnetite, which has active sorption centres [56]. In this case, it is possible to carry out chemisorption due to the formation of hydrogen bonds between the carboxyl groups and the hydrated oxide surface. The electrostatic repulsive forces arising among highly negatively charged CA-coated magnetite particles in an aqueous suspension also play an important role in the homogenous dispersion in water [50].

Fig. 3 shows the XRD patterns and FTIR spectra of MNPs fabricated in an inert atmosphere without (M2) and with (M2CA) CA. Depending on the CA addition during the synthesis, all MNPs demonstrated Bragg reflections at $30.35, 35.63, 43.49, 53.56, 57.12$ and 62.81° , corresponding to the cubic symmetry of the (220), (311), (400), (422), (511) and (440) planes of magnetite, respectively (Fig. 3A). Moreover, the calculated average crystallite size was similar for M2 ($d = 13 \pm 3$ nm) and M2CA ($d = 15 \pm 4$ nm) sizes. Therefore, there is no influence of CA addition on the magnetite synthesis in an inert atmosphere for the crystalline structure of MNPs.

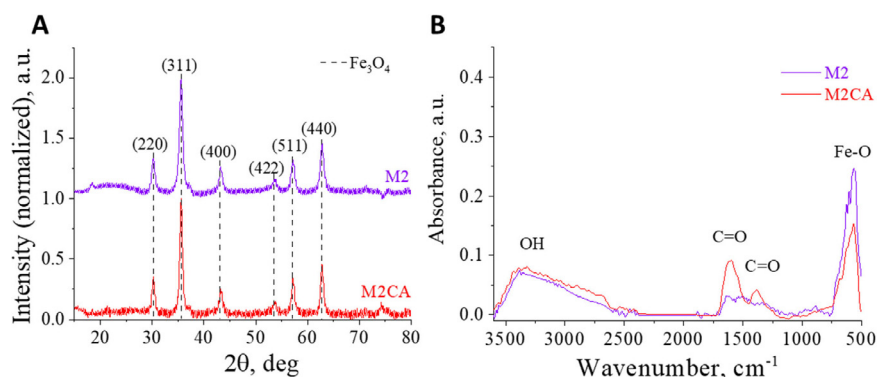


Fig. 3. (A) XRD patterns and (B) FTIR spectra of MNPs: M2 — synthesized in an inert atmosphere without the addition of CA, M2CA — synthesized in an inert atmosphere with the addition of CA.

FTIR spectra of CA-uncoated and coated MNPs exhibited typical absorption bands of magnetite at $\sim 580\text{ cm}^{-1}$ (Fe–O vibrations) and $2500\text{--}3550\text{ cm}^{-1}$ (–OH group stretching vibrations) (Fig. 3B) [50]. However, CA-coated MNPs also had bands at 1592 and 1370 cm^{-1} . The band at 1592 cm^{-1} refers to the asymmetric stretching vibrations of the COOH groups of CA and indicates the covalent binding of the CA radical to the surface of Fe₃O₄ NPs by chemisorption of the carboxylate (citrate) ions [50]. A C–O band at 1370 cm^{-1} occurs when CA is covalently bonded to the surface of iron oxide [57]. Thus, the FTIR results confirmed the successful coating of the MNPs with CA. In addition, Raman spectroscopy did not reveal a difference between MNPs without (M2) and with citric acid (M2CA) (Supporting information, Figure S1). Also, in comparison with the MNPs synthesized at room temperature and in an air atmosphere (M1, Fig. 2B), no bands of goethite were detected in the FTIR spectra of the MNPs synthesized with heating in an inert atmosphere.

In particular, some of the carboxylate groups of CA are strongly coordinated with iron cations on the Fe₃O₄ surface to form a durable coating (a possible schematic representation of CA-coated magnetite particles is shown in Fig. 4), while uncoordinated carboxylate groups penetrate into the aqueous medium, giving Fe₃O₄ a high degree of colloidal stability in an aqueous suspension.

Based on the results of the XRD analysis, FTIR and Raman spectroscopy, we have shown that the absence of oxygen in the reaction medium leads to the formation of magnetite phase-pure NPs. In contrast, NPs synthesized under air atmosphere conditions, without the protection of an inert atmosphere, are reddish-brown, indicating the presence of contamination with other iron oxides due to strong oxidation [58]. At the same time, this contamination critically reduces the magnetic properties of the iron oxide NPs [58]. Meanwhile, nitrogen gas bubbling through iron salt solutions protects MNPs against critical oxidation and reduces the particle size compared to methods without oxygen removal [36]. Thus, the use of an oxygen-free atmosphere for MNP synthesis is highly desirable to avoid the formation of oxide contamination.

3.2. Investigation of the morphology and structure of the synthesized Fe₃O₄/rGO composites

Fig. 5 shows the SEM images of Fe₃O₄/rGO composites synthesized by the co-precipitation method with various methodologies. The analysis of their size distribution revealed an average value of $60 \pm 10\text{ nm}$ for M1N/rGO (Fig. 5B), which is slightly increased compared to the surfactant-treated composite particles. Composite particles based on rGO and MNPs synthesized with CA had an average size of $47 \pm 9\text{ nm}$ (Fig. 5D). The composite

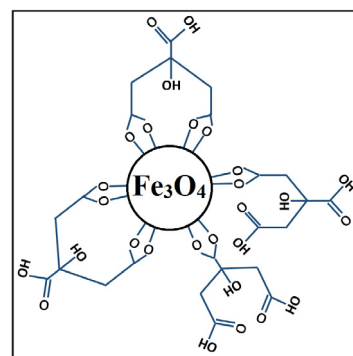


Fig. 4. Schematic representation of the covalent bonds between a magnetite particle and citrate ions.

particles M1N/rGO without a surfactant (CA) coating retain a tendency towards stronger agglomeration and aggregation. Figure S3 shows a typical SEM image of rGO (805424-1G, Sigma Aldrich), revealing that the product consists of large numbers of layers of separated ultrathin sheets with an accordion-like structure. The folding nature is clearly visible. The graphene sheets have an exfoliated form, which corresponds to the literature data [59]. Since Si substrates were used for SEM measurements, EDX analysis demonstrated that the composite particles contained iron, oxygen and carbon. The relative atomic concentrations of these elements in the composite particles were as follows: M1N/rGO — Fe of 2%, C of 82% and O of 7%, M2CA/rGO — Fe of 5%, C of 29% and O of 11%. The remaining atomic concentrations in the EDX-spectra referred to Si, which was used as substrate. The presence of C is associated with rGO-coated iron oxide. Therefore, the EDX-results revealed the formation of the Fe₃O₄/rGO composites.

Fig. 6 shows the XRD patterns of the Fe₃O₄/rGO composites synthesized with various experimental methodologies. The Fe₃O₄/rGO composites obtained by co-precipitation in an inert atmosphere exhibited the same Bragg's reflections as their precursors M1N and M2CA (Figs. 2A and 3A). At the same time, a typical rGO reflection at 24.56° was not observed in the synthesized Fe₃O₄ composites, which can be explained by the low content of rGO sheets in the Fe₃O₄/rGO composite [60]. A crucial factor in the preparation of Fe₃O₄/rGO composites is the mass ratio of the initial components used in the synthesis. In the literature, the peaks of rGO on the diffraction pattern of the Fe₃O₄/rGO composites appear only at a relatively high rGO content (more than 6:1 Fe₃O₄/rGO) [12,61].

Both FTIR spectra (Fig. 7A and C) have no absorption bands of rGO, which may indicate that no chemical bonds were formed,

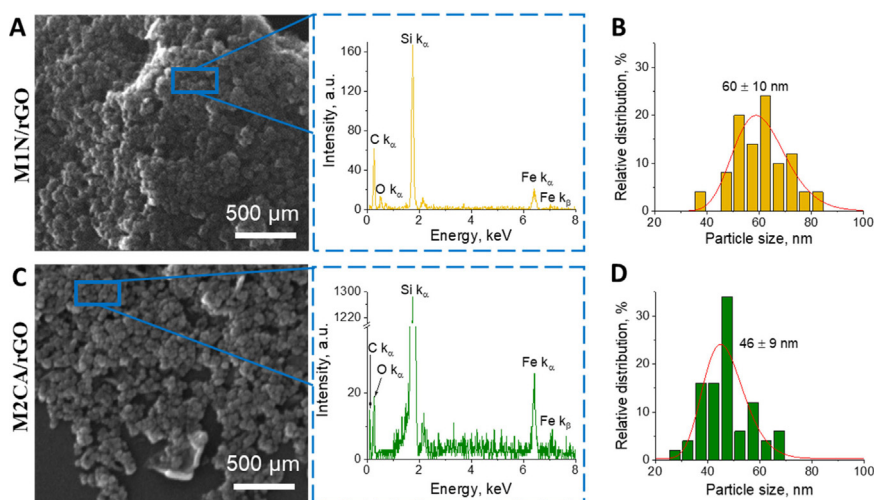


Fig. 5. (A, C) SEM images and (B, D) relative size distributions for $\text{Fe}_3\text{O}_4/\text{rGO}$ composites: (upper row) M1N/rGO — synthesized at room temperature in an inert atmosphere, (bottom row) M2CA/rGO — synthesized with heating and addition of CA in an inert atmosphere. Insets show EDX spectra collected at the mentioned area in the SEM images for the $\text{Fe}_3\text{O}_4/\text{rGO}$ composites.

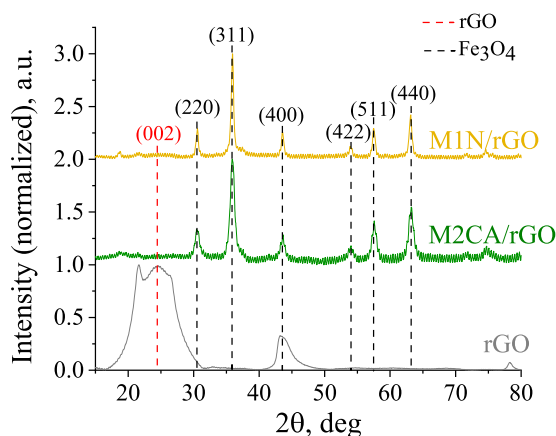


Fig. 6. XRD patterns of rGO and $\text{Fe}_3\text{O}_4/\text{rGO}$ composites: M1N/rGO — synthesized at room temperature in an inert (N_2) atmosphere, M2CA/rGO — synthesized with heating and CA in an inert (Ar) atmosphere.

resulting in physical adsorption. [62] However, the Raman spectra of the $\text{Fe}_3\text{O}_4/\text{rGO}$ composites demonstrated the presence of two characteristic peaks at 1360 and 1605 cm^{-1} corresponding to the D and G bands of rGO (Fig. 7B and D) [63]. The G band corresponds to the first-order scattering of the E_{2g} mode for sp^2 carbon domains, while the pronounced D band is associated with structural defects of carbon atoms [63,64]. Therefore, these two bands are strong evidence for the presence of rGO in the synthesized composite particles. The intensity ratio of the D and G band (I_D/I_G) can be used to determine the defect density of the MNPs/rGO composites. The I_D/I_G ratio of rGO and M2CA/rGO composites was calculated as 1.08 and 0.76, respectively. The I_D/I_G ratio in the case of the M2CA/rGO composite decreased upon addition of CA, which means that the defect density decreased [65].

XPS analysis was performed to investigate the chemical composition of the CA-functionalized MNPs and their composite with rGO (Fig. 7E–H). All typical elements corresponding to the MNPs and rGO, such as carbon, oxygen and iron, were detected (Fig. 7E). At the same time, XPS analysis revealed the difference in the relative atomic concentration of the elements between M2CA and M2CA/rGO composites. As seen, the attachment of rGO on the CA-functionalized MNPs resulted in an increased content of carbon

from 28% to 47% as well as reduction of oxygen and iron from 48% to 37% and from 23% to 16%, thereby indicating the presence of rGO in the composite.

Meanwhile, the analysis of high-resolution XPS spectra revealed clearly demonstrated the presence of CA on the surface of the MNPs (Fig. 7F–H). The C 1s region of M2CA NPs was fitted with three typical peaks corresponding to C–C/C–H, C–O and C=O from citric acid (Fig. 7F) [66]. In turn, despite the presence of C–O and C–O functional groups, the O 1s core level also demonstrated the presence of the Fe–O group arising from the MNPs (Fig. 7G) [67]. At the same time, the fitting of the Fe 2p region demonstrated the presence of Fe^{2+} and Fe^{3+} ions occupying the octahedral (denoted as Oh) and tetrahedral (denoted as Th) interstices of the cubic spinel type structure (Fig. 7H). Ideally, the atomic ratio of $\text{Fe}^{2+}:\text{Fe}^{3+}$ in magnetite is 1:2, whereas the precise ratio of $\text{Fe}_{\text{Oh}}^{2+}:\text{Fe}_{\text{Oh}}^{3+}:\text{Fe}_{\text{Th}}^{3+}$ should be 1:1:1 [67]. In turn, the developed M2CA MNPs demonstrated a slightly lower ratio of 1:0.78:0.61, which indicates the formation of a CA layer on the surface of the MNPs. A similar ratio for MNPs functionalized by CA was also reported elsewhere [67].

The attachment of rGO on the CA-functionalized MNPs resulted in the appearance of the typical peak for C sp^3 (Fig. 7F). At the same time, a pronounced increase of the C–O peak was observed in the O 1s region (Fig. 7G). These changes correspond to the contribution of rGO [68]. Additionally, there was no effect of rGO attachment on the Fe 2p state of the CA-functionalized MNPs (Fig. 7H).

Analysis of the dispersion stability of the particles and composites in water was carried out. 0.03 g of the magnetite or composite was suspended in 10 ml of distilled water and sonicated for 30 min. Further, a comparative analysis of the precipitation rate of particles at several time points was carried out. Digital pictures were taken to display the dispersion quality of Fe_3O_4 and $\text{Fe}_3\text{O}_4/\text{rGO}$ in distilled water (Fig. 8).

After 1 h of sonication, the uncoated M1N and M1N/rGO samples began to precipitate (Fig. 8B). After 3 h, precipitation became even more noticeable, especially for the M1N sample, which did not contain CA or rGO (Fig. 8C). After 24 h, the M1N sample completely precipitated, the M1N/rGO sample was still partly dispersed in suspension, while the samples coated with CA–M2CA and M2CA/rGO remained in a well-dispersed state (Fig. 8D). In view of the outstanding colloidal stability of the dispersed solutions of M2CA/rGO (Fig. 8A–D), the use of CA can be an effective approach not only to stabilize dispersed iron oxide solutions, but

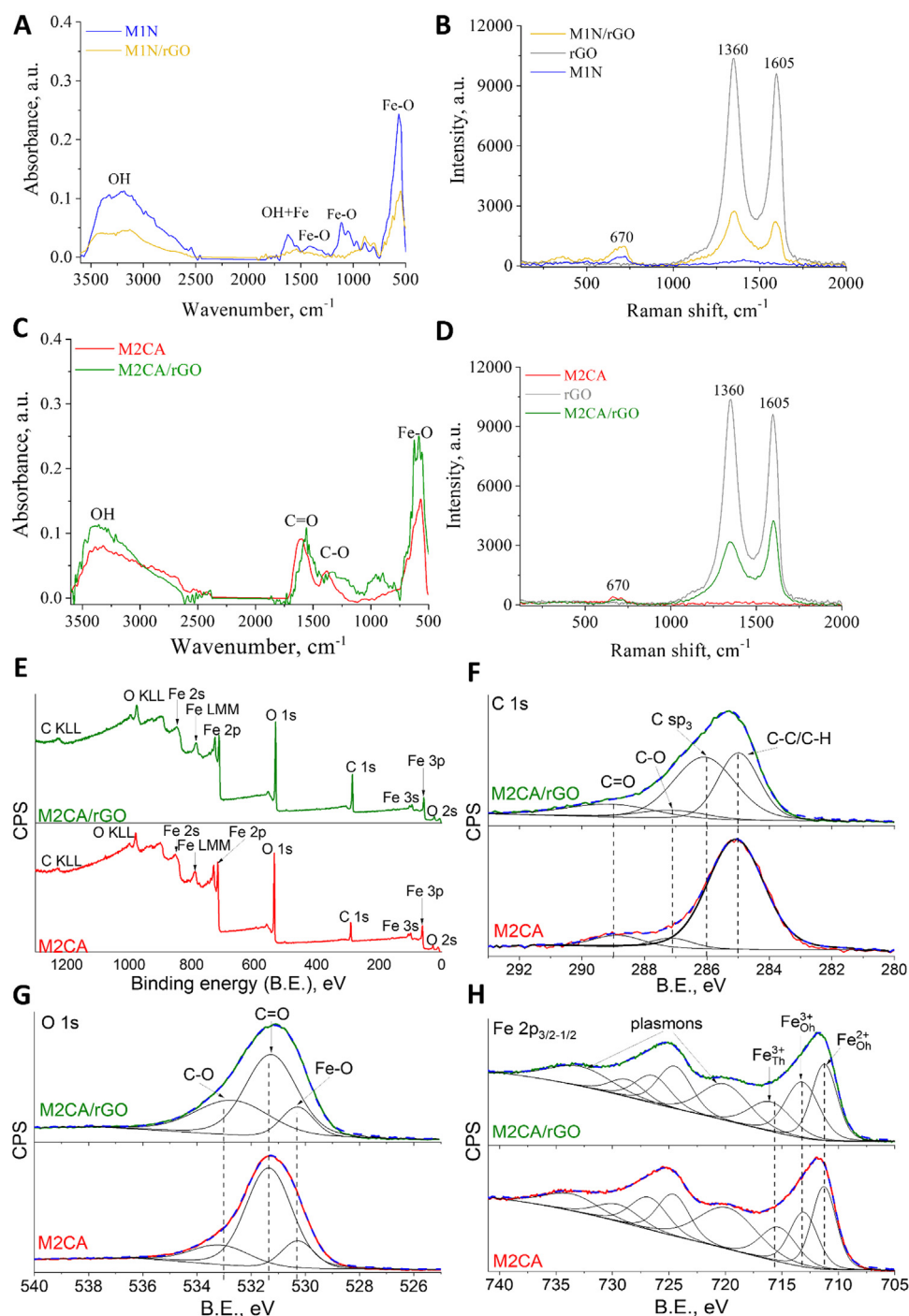


Fig. 7. (A, C) FTIR and (B, D) Raman spectra of $\text{Fe}_3\text{O}_4/\text{rGO}$ composites: M1N/rGO — synthesized at room temperature in an inert (N_2) atmosphere, M2CA/rGO — synthesized with heating and CA in an inert (Ar) atmosphere. (E) Survey and (F–H) high-resolution XPS spectra of (F) C 1s, (G) O 1s and (H) Fe 2p core levels for M2CA and M2C2/rGO NPS.

also for other composites of oxides different from magnetite and rGO. For example: ZnFe_2O_4 , $\text{Sm}_2\text{Ti}_2\text{O}_7$, ZnO , Ag-ZnO , CeO_2 and Y_2O_3 . With a successful outcome, this approach can be extended to other technological applications, such as stable photocatalysis and electrochemical nanosystems [69,70].

For a more detailed study of the size and morphology of $\text{Fe}_3\text{O}_4/\text{rGO}$ composite particles, TEM analysis was performed (Fig. 9). The TEM micrographs revealed spherical MNPs for both the M1N/rGO and M2CA/rGO composites (Fig. 9A–B). The diameter of the MNPs obtained at room temperature in a nitrogen atmosphere varied in the range from 12 to 33 nm, with a mean

size of 24 ± 4 nm (Supporting information, Figure S2C). However, the evaluated diameter of CA-coated MNPs varied in the range from 5 to 27 nm, with a mean size of 15 ± 4 nm (Supporting information, Figure S2D). It is worth noting that the CA coating of NPs improves the uniformity of the crystallite size distribution and shape. Thus, CA-coated MNPs revealed better monodispersity. In addition, the surface functionalization of MNPs with CA effectively decreases their size and coalescence between NPs seems to be prevented [71]. SEM and TEM results show significant size differences due to the better spatial resolution of the latter.

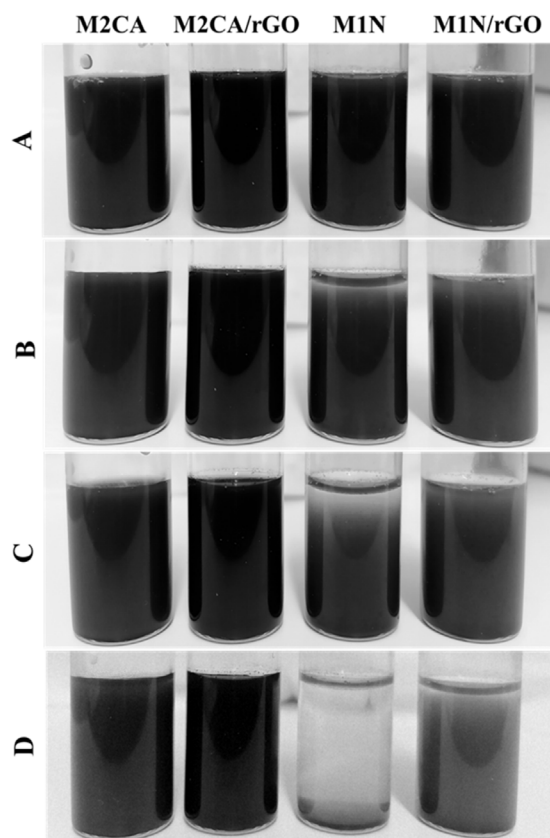


Fig. 8. The dispersion stability of Fe_3O_4 and $\text{Fe}_3\text{O}_4/\text{rGO}$ in water: A – immediately after sonication, B – 1 h after sonication, C – 3 h after sonication, and D – 24 h after sonication.

The dark-field TEM images of M1N/rGO and M2CA/rGO taken in the (311) diffraction reflex of Fe_3O_4 are shown in Fig. 9C and D, respectively. The bright spots correspond to magnetite crystals with a (311) plane orientation in M1N/rGO and M2CA/rGO. M2CA NPs are partially and randomly illuminated, indicating many crystalline defects and a polycrystalline structure. M1N NPs are characterized by a very bright and homogeneous contrast within one nanoparticle, indicating their strongly diffracting single-crystalline structure. Therefore, all the obtained MNPs in composites were a mixture of single-crystalline and polycrystalline NPs. HRTEM images of M1N/rGO and M2CA/rGO are shown in Fig. 9E and F, respectively. The HRTEM images show well-defined lattice planes of magnetite particles with perfect crystallinity. In addition, both types of $\text{Fe}_3\text{O}_4/\text{rGO}$ composite NPs exhibited continuous ring patterns with spotty diffraction rings corresponding to the (220), (311), (400), (422), (511) and (440) planes of Fe_3O_4 (Fig. 9G–H). However, M1N/rGO had clearer reflections than M2CA/rGO in the SAED images. Therefore, the M2CA/rGO sample displays the polycrystalline structure of the NPs, whereas M1N/rGO crystals are more homogeneously distributed, confirming their single-crystalline structure.

It is known that the nucleation process strongly affects the size distribution of crystals [72]. To obtain NPs with a narrow size distribution, it is necessary to create conditions under which nuclei will form simultaneously, so their subsequent growth will occur under the same conditions and crystals will be of a similar size. According to LaMer's theory [73], the process of particle formation consists of three stages: (I) a rapid increase in the concentration of a substance in a solution, (II) “burst nucleation”, which significantly reduces the amount of a substance in a solution, and (III) a growth period, which should take place in a

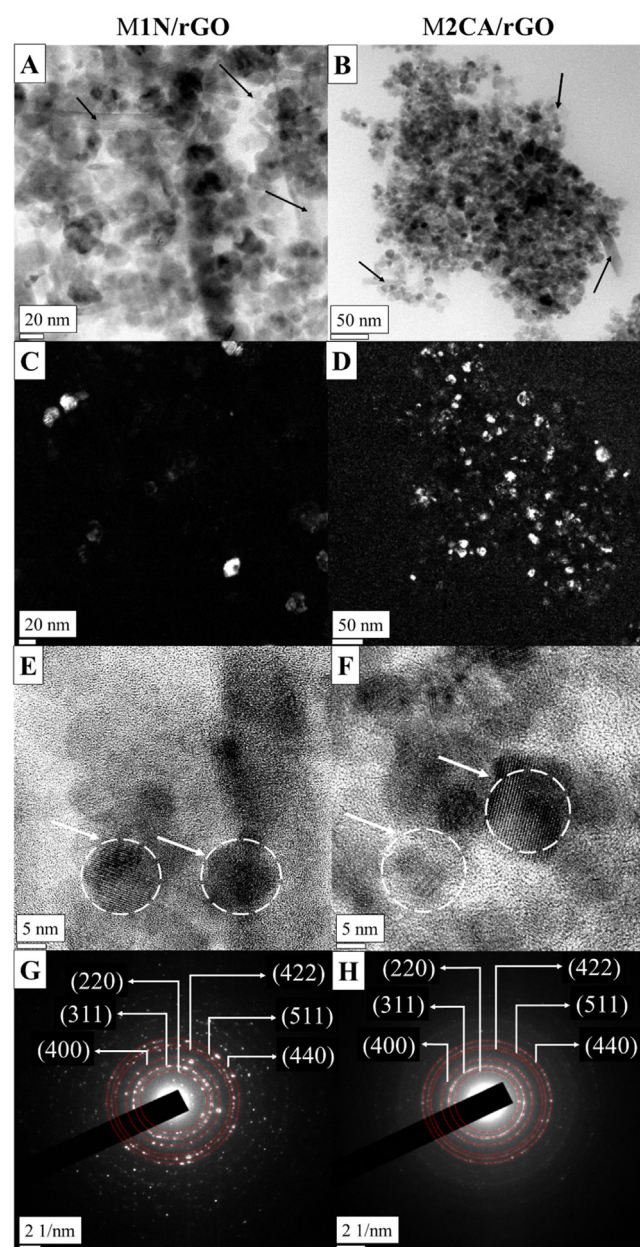


Fig. 9. TEM analysis of the composites: (A, B) bright-field TEM images, (C, D) dark-field TEM images in the (311) reflection, (E, F) high-resolution (HR) TEM images of MNPs and (G, H) selected area electron diffraction (SAED) patterns of MNPs. The nanosheets of rGO are marked with black arrows (A–B). The magnetite is marked with white arrows (E–F).

diffusion-controlled mode. However, in a real system, no matter how short the nucleation time is, at the end of the nucleation process, the particles will have a certain size distribution; high supersaturation in solution promotes not only nucleation but also the growth of the formed nuclei, which leads to an increase in the polydispersity of the crystals [74]. A decrease in polydispersity can occur in the nanoparticle growth period, which is much longer than the nucleation period in the case of “burst nucleation” [75]. The rate of crystal growth is determined by two processes – the diffusion of the substance to the surface and its deposition on the surface. In the case where deposition on the surface occurs much faster than diffusion, the growth of the crystal proceeds in a diffusion-controlled mode [76]. During the nucleation period, the number of particles increases very rapidly

and this period is accompanied by a slight broadening of the particle size distribution due to the parallel growth of already formed particles [77]. Then, a period of particle growth begins, during which the number of particles remains constant. In the diffusion-controlled mode, small particles grow faster than large particles and, at the end of this process, all particles become the same size, that is, the size distribution is narrowed [78]. The most important reaction parameters that affect the kinetics of nanoparticle formation and growth are the temperature, concentration of reagents, pH and ionic strength of the solution [79]. Thus, by controlling the nucleation rate and nuclear growth rate, monodisperse MNPs samples with different sizes of particles can be synthesized.

For the fabrication of the $\text{Fe}_3\text{O}_4/\text{rGO}$ composite in this study, rGO sheets were modified in NaOH. The presence of hydroxyl groups creates an additional negative charge on the rGO surface, which is very important in its efficient decoration with Fe_3O_4 [34]. As a result, the monodisperse Fe_3O_4 NPs were homogeneously anchored to rGO on both sides of the wrinkled surface. Additionally, it can be assumed that anchoring of the Fe_3O_4 crystals to rGO sheets is mediated by the residual oxygen groups of the latter [27]. As a result, due to the incomplete reduction of rGO, a negative surface charge persists through rGO hydrophilic functional groups (epoxy, carboxyl and hydroxyl) on its surface. The positively charged Fe^{2+} and Fe^{3+} ions are effectively fixed on the negatively charged rGO surface due to electrostatic interactions and strong van der Waals interactions at the boundaries of the rGO nanosheets [80]. Thus, the large surface area of rGO, its increased interlayer spacing and the availability of a large number of evenly distributed active sites are very useful for the efficient anchoring of MNPs [29].

It is also known that the surface of magnetite is multifunctional and reveals oxidizing sites ($\text{O}_2(\text{ads})$, O^{2-} , O^-), donor sites (charged oxygen vacancies), Lewis acid sites (coordinately unsaturated Fe^{2+} and Fe^{3+} cations), Brønsted sites (OH groups), base sites (hydroxyl groups OH, $\text{Fe}-\text{OH}$) and surface oxygen anions (O^{2-}) [81]. When modifying the surface of magnetite, citric acid (CA) interacts with its Brønsted centres (OH groups). The bonding of rGO with magnetite may occur through donor-acceptor interactions with the Lewis centres of magnetite (Fe^{2+} , Fe^{3+}) [28]. Thus, the functionalization of magnetite with CA does not prevent or hinder the interaction of magnetite with rGO, since the interactions occur at different active centres of the iron oxide bifunctional surface (Lewis and Brønsted centres). CA, as a stabilizer of MNPs, may be covalently attached to rGO. It has been reported that a nanocomposite of GO functionalized with CA was successfully synthesized [82]. FTIR results confirmed the interface bonding between GO and CA in the nanocomposite. The typical peak of the O–H group from GO at 3392 cm^{-1} was reduced and shifted to 3431 cm^{-1} due to the contribution of aliphatic carboxylic groups from CA. Thus, CA may affect the structure of rGO.

3.3. The results on samples magnetization

The magnetic properties of the investigated MNPs and $\text{Fe}_3\text{O}_4/\text{rGO}$ composites are particularly important for biomedical applications. Due to the magnetic properties, it is possible to localize treatment or transport drugs by applying a magnetic field. The main magnetic property of ferromagnetic materials is saturation magnetization, which is characterized by the ordering of all magnetic moments within the material. The magnetization of MNPs and $\text{Fe}_3\text{O}_4/\text{rGO}$ composites was investigated at a temperature of 300 K with an external magnetic field from 0 to 6.5 kOe. Fig. 10 shows the magnetization curves for all the synthesized NPs in the present study.

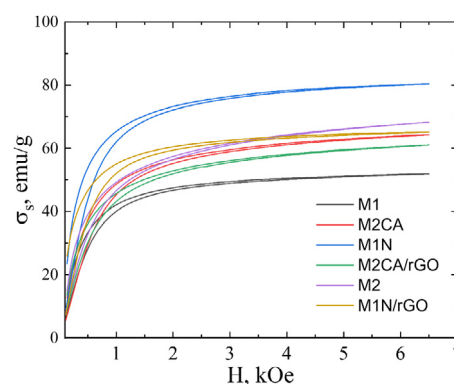


Fig. 10. Magnetization results obtained for pure magnetite and $\text{Fe}_3\text{O}_4/\text{rGO}$ composite nanoparticles.

Table 2

Relative atomic concentrations of the observed element on the surface for M2CA and M2CA/rGO NPs.

Composite NPs	Relative atomic concentration, %		
	C 1s	O 1s	Fe 2p
M2CA	29	48	23
M2CA/rGO	47	37	16

Pure MNPs obtained in inert atmospheres, such as nitrogen (M1N – 80.27 emu/g) and argon (M2 – 68.25 emu/g), exhibited the highest saturation magnetization among the other MNPs and $\text{Fe}_3\text{O}_4/\text{rGO}$ composite NPs (Table 2). These results are slightly lower than those of the bulk material (92 emu/g) [83]. The decrease in magnetization can be caused by such factors as the presence of canted spins in the surface layer, as well as the behavior of the spins of the surface layer similar to spin glasses, or the presence of a magnetically degenerated layer [84]. All the NPs also had ferromagnetic behaviour with a hysteresis loop, which is typical for MNPs larger than 10 nm [85]. The lack of magnetization saturation in high magnetic fields is due to the small particle size and large surface area, which leads to some spin canting. Upon further functionalization of the MNPs by adding CA (M2CA), a decrease in magnetization ($\sigma_s = 64.1$ emu/g) occurred due to the formation of a surfactant layer on the MNP surface [45]. The decrease in magnetization is also affected by the phase composition of the sample. In the case of MNPs synthesized under ambient conditions, M1 had the lowest magnetization ($\sigma_s = 51.9$ emu/g) due to the inclusion of impurities [86] such as non-magnetic goethite (Fig. 2), resulting in an increased nanoparticle size (Table 2). The addition of rGO with a $\text{Fe}_3\text{O}_4/\text{rGO}$ ratio of 6:1 also leads to a slight decrease in the saturation magnetization of the MNPs, which is explained by the lower content of the magnetic phase in the composite [61]. It is known that nanoscale magnetization also decreases with decreasing crystallite size [87]. The magnetization value for the M2CA/rGO composite with a crystallite size of 11 ± 3 nm was 61 emu/g, whereas the magnetization for the M1N/rGO composite with a crystallite size of 23 ± 3 nm was higher ($\sigma_s = 65.0$ emu/g). However, the observed decrease can also be due to the formation of a surface-active layer of oxygen groups due to the addition of CA. According to literature data, the saturation magnetization of magnetic particles of iron oxide used for biomedical applications is in the range from 30 to 80 emu/g [88–90]. The MNPs obtained in this work exhibit saturation magnetization within this range and therefore could be used in biomedicine in the future (see Table 3).

The developed $\text{Fe}_3\text{O}_4/\text{rGO}$ composites are promising as fillers in 3D polymer scaffolds, especially those based on piezoelectric

Table 3

A summary of the saturation magnetization, particles and crystallite size values for the synthesized pure and composite MNPs.

Sample	Composition	Fe ₃ O ₄ /rGO ratio	σ_s , emu/g	σ_s , kA/m	Particle size, nm	Crystallite size, nm
M1	Fe ₃ O ₄	–	51.90	259.50	74 ± 12	40 ± 12
M2	Fe ₃ O ₄	–	68.25	292.79	46 ± 10	13 ± 3
M1N	Fe ₃ O ₄	–	80.27	401.35	46 ± 8	16 ± 5
M2CA	Fe ₃ O ₄	–	64.10	320.50	47 ± 9	15 ± 3
M1N/rGO	rGO/Fe ₃ O ₄	6:1	64.97	278.72	61 ± 10	23 ± 3
M2CA/rGO	rGO/Fe ₃ O ₄	6:1	60.96	261.52	46 ± 9	11 ± 3

polymers. Recently, the efficiency of rGO filler for the improvement of the piezoresponse of 3D biodegradable scaffolds for regenerative medicine has been demonstrated [91]. The influence of both rGO and GO on the structure of the piezopolymer has been shown in the literature [91,92]. However, polymers are mostly semicrystalline materials consisting of a non-piezoelectric amorphous phase. In contrast to GO, rGO is a conductive or semiconductive material, depending on the degree of reduction or modifications (e.g. doping with N) [93,94]. Therefore, rGO fillers can promote the enhanced piezoresponse of 3D scaffolds based on dielectric polymers [95]. In this regard, future research on composite fillers based on the conductive rGO and magnetic MNPs are prospective to tailor a piezoresponse via an external magnetic field. Moreover, variation of the ratio between rGO and MNPs in the composite filler enables control over the magnetization of the 3D polymer scaffolds.

3.4. Cell culture results

To examine the feasibility of the obtained MNPs and composites in bio-related fields, their cytotoxicity was investigated. The effect of the samples on cell viability was assessed with MSCs by means of an MTT assay. To determine the cytotoxicity of the magnetite and composite particles, solutions containing different concentrations of each sample were diluted in growth medium. The cell viability was determined on the 1st and 3rd days, and the number of cells cultivated without samples was taken as 100% (Fig. 11).

The results obtained in our study revealed that all the materials are biocompatible. As a result of the cytotoxicity test on all samples at various concentrations, only M1N revealed an IC₅₀ (half maximum inhibitory concentration) at a concentration of 100 µg/mL after incubation with cells for 3 days [96]; however, at lower concentrations, such as 33, 10, 3 and 1 µg/mL, cytotoxicity was not observed, and the number of cells statistically did not differ from that incubated without particles (control). In other cases (Fig. 11), the number of viable cells, even at high concentrations of the magnetite NPs, did not decrease by 80% either on the first day of incubation or on the third day, which indicates that these concentrations are not cytotoxic [97], except for sample M1N/rGO, which dropped to 70% at a concentration of 100 µg/mL on day 3. Since CA is one of the products of TCAC, a normal metabolic process in the human body [54], CA-coated MNPs are remarkably biocompatible, which makes them promising candidates for applications in various bio-related fields.

Nowadays, many techniques using magnetite nanoparticles and graphene oxide have been developed to improve the efficiency of tissue regeneration and in other bio-related fields [98–100]. In this regard, much attention is paid to their cytotoxicity [33,101,102]. Recent reports on the biomedical applications of magnetite/graphene-derived composites and the results of cell toxicity reported in literature are summarized in Table S1. The physicochemical properties of magnetic graphene oxide, biocompatibility tests *in vitro* and *in vivo*, and its biomedical applications are well described in a recent review [103].

It is reported that rGO induced cytotoxicity, apoptosis and oxidative stress [33]. Thus, much attention is paid to cytotoxicity studies of graphene-based derivatives [101,102]. It has been

shown that magnetites and different composites of magnetites have dose- and time-dependent cytotoxicity effects with various mechanisms, as described in the study [102]. For example, the concentration of Fe₃O₄ nanoparticles does not show cytotoxicity up to 100 µg/mL [104], but cobalt-ferrite nanoparticles with a concentration higher than 40 µg/mL start to show cytotoxicity effects [105]. GO caused an antibacterial effect and cytotoxicity by different mechanisms, as described in the study [101]. In turn, rGO does not show cytotoxicity effects on cells at concentrations lower than 50 µg/mL [106,107]. Good biocompatibility is also reported in case of other composites, such as polymer-based composites doped with rGO [100]. Good biocompatibility of poly(trimethylene carbonate) scaffolds with rGO is also demonstrated using PC-12 neuroblastoma cells [108]. The cell viability slightly decreased on addition of graphene in composites with magnetites after 48 h of incubation, with the concentration of the composite being 1000 µg/mL [109].

The physicochemical properties and biocompatibility of magnetic graphene oxide *in vitro* and *in vivo*, and its biomedical applications are described elsewhere [103]. In general, it is reported that Fe₃O₄/graphene nanocomposites reveal a high level of biocompatibility after cell treatment with the dosage of 80 µg/mL [110] and 221 µg/mL, 109. No significant difference in viability, proliferation, apoptotic activity and necrotic ability potential of DPSCs is revealed in the case of nGO@Fe₃O₄ MNPs after 2 days incubation at a concentration of 100 µg/mL [111]. Concerning the cytotoxicity results obtained in this study, on addition of magnetite NPs into polymer matrices, the prepared hybrid material should also not provide cytotoxic effects. The results of the cell culture study will be used to define the content of magnetite to be added to polymer matrices to prepare magnetoactive scaffolds by electrospinning as the next step of research.

4. Conclusions

In this work, MNPs and Fe₃O₄/rGO biocomposites with a high saturation magnetization were successfully synthesized. MNPs were coated with CA to reduce their agglomeration. The FTIR results confirmed the functionalization of the MNPs with CA. It is also found that the CA coating decreases the size of the NPs. Based on the XRD patterns, FTIR and Raman spectra, the formation of phase-pure MNPs requires the use of an oxygen-free atmosphere during synthesis. The Raman study infers the successful formation of Fe₃O₄/rGO composites. SEM analysis revealed spherical MNPs with sizes from 46 to 74 nm. TEM analysis showed that the obtained MNPs deposited on rGO sheets were a mixture of single-crystalline and polycrystalline NPs. The best magnetization saturation values were shown by MNPs synthesized in an oxygen-free atmosphere without the use of CA (σ_s = 80.27 emu/g). The CA coating led to a slight decrease in the magnetization (σ_s = 64.1 emu/g), which was associated with the formation of a surface-active layer on the MNP surface. The Fe₃O₄/rGO composites also reveal a reduced saturation magnetization of σ_s = 60.96 emu/g, which is associated with a decrease in the content of the magnetic phase in the Fe₃O₄/rGO composite. The bonding mechanism between Fe₃O₄ and rGO nanosheets is electrostatic and van der Waals interactions. An *in vitro* cytotoxicity study

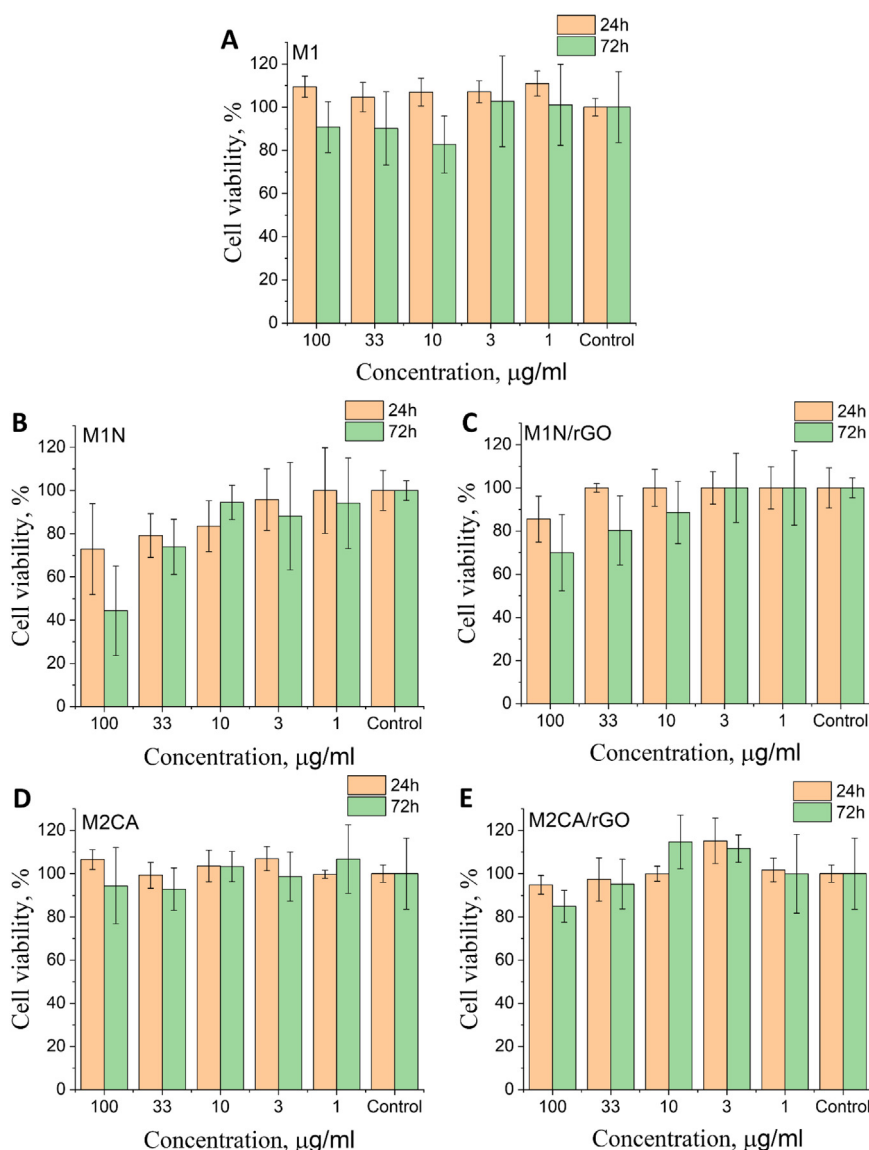


Fig. 11. 1. Cytotoxicity results obtained for different magnetite and composite samples: (A) M1, (B) M1N, (C) M1N/rGO, (D) M2CA, and (E) M2CA/rGO.

showed that the number of viable cells, even at high concentrations of magnetite NPs, did not decrease by 80% either on the first day of incubation or on the third day, which indicates that these concentrations are not cytotoxic. The synthesized MNPs and $\text{Fe}_3\text{O}_4/\text{rGO}$ composites are expected to be useful for biomedical applications, due to their excellent magnetic properties and biocompatibility, and to serve as magnetic fillers for hybrid polymer matrices followed by external magnetic field exposure to control cellular behaviour via strain-mediated effects within the polymer matrices.

CRediT authorship contribution statement

Yulia R. Mukhortova: Conceptualization, Methodology, Investigation, Writing – original draft, Visualization. **Artyom S. Pryadko:** Conceptualization, Methodology, Investigation, Writing – original draft, Visualization. **Roman V. Chernozem:** Conceptualization, Methodology, Investigation, Writing – original draft, Visualization. **Igor O. Pariy:** Methodology, Investigation, Writing – original draft, Visualization. **Elizaveta A. Akoulina:** Methodology, Investigation. **Irina V. Demianova:** Methodology, Investigation. **Irina I. Zharkova:** Methodology, Investigation. **Yurii**

F. Ivanov: Investigation. **Dmitriy V. Wagner:** Investigation. **Anton P. Bonartsev:** Conceptualization, Resources, Writing – review & editing, Supervision, Project administration. **Roman A. Surmenev:** Conceptualization, Resources, Writing – review & editing, Supervision, Project administration. **Maria A. Surmeneva:** Conceptualization, Resources, Writing – review & editing, Supervision, Project administration.

Declaration of competing interest

The authors declare that they have no known competing financial interests or personal relationships that could have appeared to influence the work reported in this paper.

Acknowledgements

The research was conducted at Tomsk Polytechnic University within the aid of a Tomsk Polytechnic University Competitiveness Enhancement Program grant. The authors acknowledge the support of this study from Sergey Sinyavskiy and Ekaterina Karpenko. In vitro assays were conducted at the M.V. Lomonosov Moscow State University, Faculty of Biology. This work is supported by

the Russian Science Foundation (project number 20-63-47096, materials, properties investigation). Financial support from the Ministry of Science and Higher Education of the Russian Federation is acknowledged (grant agreement #075-15-2021-588 from 1.06.2021, measurements of magnetic properties, structure analysis, FTIR study).

Appendix A. Supplementary data

Supplementary material related to this article can be found online at <https://doi.org/10.1016/j.nanoso.2022.100843>.

References

- [1] Z.R. Stephen, F.M. Kievit, M. Zhang, Magnetite nanoparticles for medical MR imaging, *Mater. Today* 14 (2011) 330–338.
- [2] P. Majewski, B. Thierry, Functionalized magnetite nanoparticles—synthesis, properties, and bio-applications, *Crit. Rev. Solid State Mater. Sci.* 32 (2007) 203–215.
- [3] Y.-w. Jun, Y.-M. Huh, J.-s. Choi, J.-H. Lee, H.-T. Song, S. Kim, S. Yoon, K.-S. Kim, J.-S. Shin, J.-S. Suh, Nanoscale size effect of magnetic nanocrystals and their utilization for cancer diagnosis via magnetic resonance imaging, *J. Am. Chem. Soc.* 127 (2005) 5732–5733.
- [4] J.-H. Lee, Y.-M. Huh, Y.-w. Jun, J.-w. Seo, J.-t. Jang, H.-T. Song, S. Kim, E.-J. Cho, H.-G. Yoon, J.-S. Suh, Artificially engineered magnetic nanoparticles for ultra-sensitive molecular imaging, *Nat. Med.* 13 (2007) 95–99.
- [5] T. Neuberger, B. Schöpf, H. Hofmann, M. Hofmann, B. Von Rechenberg, Superparamagnetic nanoparticles for biomedical applications: possibilities and limitations of a new drug delivery system, *J. Magn. Magn. Mater.* 293 (2005) 483–496.
- [6] B. Jayadevan, Present status and prospects of magnetite nanoparticles-based hyperthermia, *J. Ceram. Soc. Jpn.* 118 (2010) 391–401.
- [7] S.O. Aisida, A. Ali, O.E. Oyewande, I. Ahmad, A. Ul-Hamid, T.-k. Zhao, M. Maaza, F.I. Ezema, Biogenic synthesis enhanced structural, morphological, magnetic and optical properties of zinc ferrite nanoparticles for moderate hyperthermia applications, *J. Nanopart. Res.* 23 (2021) 1–14.
- [8] A. Ito, M. Fujioka, T. Yoshida, K. Wakamatsu, S. Ito, T. Yamashita, K. Jimbow, H. Honda, 4-s-cysteaminylphenol-loaded magnetite cationic liposomes for combination therapy of hyperthermia with chemotherapy against malignant melanoma, *Cancer Sci.* 98 (2007) 424–430.
- [9] S.O. Aisida, P.A. Akpa, I. Ahmad, T.-k. Zhao, M. Maaza, F.I. Ezema, Bio-inspired encapsulation and functionalization of iron oxide nanoparticles for biomedical applications, *Eur. J. Inorg. Chem.* 2020 (2020) 109371.
- [10] L. Giraldo, A. Erto, J.C. Moreno-Piraján, Magnetite nanoparticles for removal of heavy metals from aqueous solutions: synthesis and characterization, *Adsorption* 19 (2013) 465–474.
- [11] S. Berensmeier, Magnetic particles for the separation and purification of nucleic acids, *Appl. Microbiol. Biotechnol.* 73 (2006) 495–504.
- [12] C.-L. Liang, Y. Liu, R.-Y. Bao, Y. Luo, W. Yang, B.-H. Xie, M.-B. Yang, Effects of Fe₃O₄ loading on the cycling performance of Fe₃O₄/rGO composite anode material for lithium ion batteries, *J. Alloys Compd.* 678 (2016) 80–86.
- [13] Y. Suo, Q.-Q. Zhao, J.-K. Meng, J. Li, X.-C. Zheng, X.-X. Guan, Y.-S. Liu, J.-M. Zhang, Fabrication and electrochemical properties of 3D Fe₃O₄@ graphene aerogel composites as lithium-ion battery anodes, *Mater. Lett.* 174 (2016) 36–39.
- [14] L. Shen, Y. Qiao, Y. Guo, S. Meng, G. Yang, M. Wu, J. Zhao, Facile co-precipitation synthesis of shape-controlled magnetite nanoparticles, *Ceram. Int.* 40 (2014) 1519–1524.
- [15] X.-M. Liu, J.-K. Kim, Solvothermal synthesis and magnetic properties of magnetite nanoplatelets, *Mater. Lett.* 63 (2009) 428–430.
- [16] A.H. Yusoff, M.N. Salimi, M.F. Jamlos, A review: Synthetic strategy control of magnetite nanoparticles production, *Adv. Nano Res.* 6 (2018) 1.
- [17] M.C. Mascolo, Y. Pei, T.A. Ring, Room temperature co-precipitation synthesis of magnetite nanoparticles in a large pH window with different bases, *Materials* 6 (2013) 5549–5567.
- [18] L.S. Ganapathé, M.A. Mohamed, R. Mohamad Yunus, D.D. Berhanuddin, Magnetite (Fe₃O₄) nanoparticles in biomedical application: From synthesis to surface functionalisation, *Magnetochemistry* 6 (2020) 68.
- [19] X. Wang, B. Guo, W. Fu, H. Yang, Triethylenetetramine promoted rGO-Fe₃O₄ nanocomposites for highly efficient Fenton-like reaction, *J. Water Process. Eng.* 31 (2019) 100814.
- [20] X. Shen, Q. Wang, W. Chen, Y. Pang, One-step synthesis of water-dispersible cysteine functionalized magnetic Fe₃O₄ nanoparticles for mercury(II) removal from aqueous solutions, *Appl. Surf. Sci.* 317 (2014) 1028–1034.
- [21] H. Cohen, A. Gedanken, Z. Zhong, One-step synthesis and characterization of ultrastable and amorphous Fe₃O₄ colloids capped with cysteine molecules, *J. Phys. Chem.* 112 (2008) 15429–15438.
- [22] M. Răduci, D. Creangă, A. Airinei, Citric-acid-coated magnetite nanoparticles for biological applications, *Eur. Phys. J. E* 21 (2006) 117–121.
- [23] H. Shen, L. Zhang, M. Liu, Z. Zhang, Biomedical applications of graphene, *Theranostics* 2 (2012) 283.
- [24] X. Sun, Z. Liu, K. Welscher, J.T. Robinson, A. Goodwin, S. Zaric, H. Dai, Nano-graphene oxide for cellular imaging and drug delivery, *Nano Res.* 1 (2008) 203–212.
- [25] W. Hu, C. Peng, W. Luo, M. Lv, X. Li, D. Li, Q. Huang, C. Fan, Graphene-based antibacterial paper, *ACS Nano* 4 (2010) 4317–4323.
- [26] O. Akhavan, E. Ghaderi, Toxicity of graphene and graphene oxide nanowalls against bacteria, *ACS Nano* 4 (2010) 5731–5736.
- [27] Y. Tang, H. Guo, L. Xiao, S. Yu, N. Gao, Y. Wang, Synthesis of reduced graphene oxide/magnetite composites and investigation of their adsorption performance of fluoroquinolone antibiotics, *Colloids Surf. A* 424 (2013) 74–80.
- [28] R. Hatel, M. Khenfouch, M. Baitoul, M. Maaza, Spectroscopic investigations of graphene derivatives coated with nanostructured Fe₃O₄, *Appl. Phys. A* 120 (2015) 1069–1074.
- [29] Y. Zhu, S. Murali, W. Cai, X. Li, J.W. Suk, J.R. Potts, R.S. Ruoff, Graphene and graphene oxide: synthesis, properties, and applications, *Adv. Mater.* 22 (2010) 3906–3924.
- [30] Y. Qin, M. Long, B. Tan, B. Zhou, Rb adsorption performance of magnetic adsorbent Fe₃O₄/RGO composite and its regeneration through a fenton-like reaction, *Nanomicro Lett.* 6 (2014) 125–135.
- [31] A.K. Das, S. Sahoo, P. Arunachalam, S. Zhang, J.-J. Shim, Facile synthesis of Fe₃O₄ nanorod decorated reduced graphene oxide (RGO) for supercapacitor application, *RSC Adv.* 6 (2016) 107057–107064.
- [32] M. Nasrollahzadeh, M. Maham, A. Rostami-Vartooni, M. Bagherzadeh, S.M. Sajadi, Barberry fruit extract assisted in situ green synthesis of Cu nanoparticles supported on a reduced graphene oxide-Fe₃O₄ nanocomposite as a magnetically separable and reusable catalyst for the O-arylation of phenols with aryl halides under ligand-free conditions, *RSC Adv.* 5 (2015) 64769–64780.
- [33] M. Ahamed, M.J. Akhtar, M. Khan, Investigation of cytotoxicity, apoptosis, and oxidative stress response of Fe₃O₄-RGO nanocomposites in human liver HepG2 cells, *Materials* 13 (2020) 660.
- [34] S. Sajjad, S.A.K. Leghari, N. Jabeen, N. Riaz, M. Tariq, I. Ahmed, M. Maaza, Fe₃O₄ nanorods r-GO sheets nanocomposite visible photo catalyst, *Mater. Res. Express* 6 (2019) 065013.
- [35] J. Li, D. Li, S. Zhang, H. Cui, C. Wang, Analysis of the factors affecting the magnetic characteristics of nano-Fe₃O₄ particles, *Sci. Bull.* 56 (2011) 803–810.
- [36] A.K. Gupta, S. Wells, Surface-modified superparamagnetic nanoparticles for drug delivery: preparation, characterization, and cytotoxicity studies, *IEEE Trans. Nanobiosci.* 3 (2004) 66–73.
- [37] A. Goodarzi, Y. Sahoo, M. Swihart, P. Prasad, Aqueous Ferrofluid of Citric Acid Coated Magnetite Particles, Vol. 789, MRS Online Proceedings Library (OPL), 2003.
- [38] D. Li, M.B. Müller, S. Gilje, R.B. Kaner, G.G. Wallace, Processable aqueous dispersions of graphene nanosheets, *Nat. Nanotechnol.* 3 (2008) 101–105.
- [39] A.R. West, Solid State Chemistry and its Applications, John Wiley & Sons, 2014.
- [40] B.D. Cullity, Elements of X-Ray Diffraction, Addison-Wesley Publishing, 1956.
- [41] V.Y. Kreslin, E. Naiden, Automatic complex for a study of the characteristics of hard magnetic materials, *J. Instrum. Exp. Tech.* 45 (2002) 55–57.
- [42] A.V. Volkov, A.A. Muraev, I.I. Zharkova, V.V. Voinova, E.A. Akoulina, V.A. Zhukov, D.D. Khaydapova, D.V. Chesnokova, K.A. Menshikh, A.A. Dudun, Poly (3-hydroxybutyrate)/hydroxyapatite/alginate scaffolds seeded with mesenchymal stem cells enhance the regeneration of critical-sized bone defect, *Mater. Sci. Eng. C* 114 (2020) 110991.
- [43] A.M. Jubb, H.C. Allen, Vibrational spectroscopic characterization of hematite, maghemite, and magnetite thin films produced by vapor deposition, *ACS Appl. Mater. Interfaces* 2 (2010) 2804–2812.
- [44] R.M. Cornell, U. Schwertmann, The Iron Oxides: Structure, Properties, Reactions, Occurrences and Uses, John Wiley & Sons, 2003.
- [45] E. Vaytulevich, T. Yurmazova, H.T. Tuan, Sorbents based on magnetite nanoparticles for biomedical applications, *Nanotechnol. Russ.* 14 (2019) 33–40.
- [46] M.A. Legodi, D. de Waal, The preparation of magnetite, goethite, hematite and maghemite of pigment quality from mill scale iron waste, *Dyes Pigm.* 74 (2007) 161–168.
- [47] A. Bahadur, A. Saeed, M. Shoaib, S. Iqbal, M.I. Bashir, M. Waqas, M.N. Hussain, N. Abbas, Eco-friendly synthesis of magnetite (Fe₃O₄) nanoparticles with tunable size: dielectric, magnetic, thermal and optical studies, *Mater. Chem. Phys.* 198 (2017) 229–235.

- [48] S.J. Iyengar, M. Joy, C.K. Ghosh, S. Dey, R.K. Kotnala, S. Ghosh, Magnetic, X-ray and Mössbauer studies on magnetite/maghemite core-shell nanostructures fabricated through an aqueous route, *RSC Adv.* 4 (2014) 64919–64929.
- [49] C.R. Nangah, T.G. Merlain, N.J. Nsami, C.P. Tubwoh, J. Foba-Tendo, K.J. Mbadcam, Synthesized goethite and natural iron oxide as effective absorbents for simultaneous removal of Co(II) and Ni(II) ions from water, *J. Encapsulation Adsorpt. Sci.* 9 (2019) 127–147.
- [50] S. Nigam, K. Barick, D. Bahadur, Development of citrate-stabilized Fe₃O₄ nanoparticles: conjugation and release of doxorubicin for therapeutic applications, *J. Magn. Magn. Mater.* 323 (2011) 237–243.
- [51] M.A. Legodi, D. de Waal, The preparation of magnetite, goethite, hematite and maghemite of pigment quality from mill scale iron waste, *Dyes Pigm.* 74 (2007) 161–168.
- [52] L.B. Salviano, T.M.d.S. Cardoso, G.C. Silva, M.S.S. Dantas, A.d.M. Ferreira, Microstructural assessment of magnetite nanoparticles (Fe₃O₄) obtained by chemical precipitation under different synthesis conditions, *J. Mater. Res.* 21 (2018).
- [53] F. Froment, A. Tournié, P. Colomban, Raman identification of natural red to yellow pigments: ochre and iron-containing ores, *J. Raman Spectrosc.* 39 (2008) 560–568.
- [54] L.V. Thomas, U. Arun, S. Remya, P.D. Nair, A biodegradable and biocompatible PVA–citric acid polyester with potential applications as matrix for vascular tissue engineering, *J. J. Mater. Sci. Mater. Med.* 20 (2009) 259–269.
- [55] J. Sato, M. Kobayashi, H. Kato, T. Miyazaki, M. Kakihana, Hydrothermal synthesis of magnetite particles with uncommon crystal facets, *J. Asian Ceram. Soc.* 2 (2014) 258–262.
- [56] X. Wang, G. Li, K.H. Row, Magnetic graphene oxide modified by imidazole-based ionic liquids for the magnetic-based solid-phase extraction of polysaccharides from brown alga, *J. Sep. Sci.* 40 (2017) 3301–3310.
- [57] M. Miola, S. Ferraris, F. Pirani, C. Multari, E. Bertone, K.Ž. Rožman, N. Kostevšek, E. Verné, Reductant-free synthesis of magnetoplasmonic iron oxide-gold nanoparticles, *Ceram. Int.* 43 (2017) 15258–15265.
- [58] Z. Liu, H. Wang, Q. Lu, G. Du, L. Peng, Y. Du, S. Zhang, K. Yao, Synthesis and characterization of ultrafine well-dispersed magnetic nanoparticles, *J. Magn. Magn. Mater.* 283 (2004) 258–262.
- [59] O. Bajjou, P.N. Mongwaketsi, M. Khenfouch, A. Bakour, M. Baïtoul, M. Maaza, J.W. Venturini, Photoluminescence quenching and structure of nanocomposite based on graphene oxide layers decorated with nanostructured porphyrin, *Nanomater. Nanotechnol.* 5 (2015) 7.
- [60] R. Madhuvilakku, S. Alagar, R. Mariappan, S. Piraman, Green one-pot synthesis of flowers-like Fe₃O₄/rGO hybrid nanocomposites for effective electrochemical detection of riboflavin and low-cost supercapacitor applications, *Sens. Actuators B* 253 (2017) 879–892.
- [61] T. Peik-See, A. Pandikumar, L.H. Ngee, H.N. Ming, C.C. Hua, Magnetically separable reduced graphene oxide/iron oxide nanocomposite materials for environmental remediation, *Catal. Sci. Technol.* 4 (2014) 4396–4405.
- [62] B. Saiphaneendra, T. Saxena, S.A. Singh, G. Madras, C. Srivastava, Synergistic effect of co-existence of hematite (α -Fe₂O₃) and magnetite (Fe₃O₄) nanoparticles on graphene sheet for dye adsorption, *J. Environ. Chem. Eng.* 5 (2017) 26–37.
- [63] V. Chandra, J. Park, Y. Chun, J.W. Lee, I.-C. Hwang, K.S. Kim, Water-dispersible magnetite-reduced graphene oxide composites for arsenic removal, *ACS Nano* 4 (2010) 3979–3986.
- [64] M. Khenfouch, M. Baïtoul, M. Maaza, Raman study of graphene/nanostructured oxides for optoelectronic applications, *Opt. Mater.* 36 (2013) 27–30.
- [65] Y.B. Kantaş, E. Erçarıkçı, M. Alanyalıoğlu, Fabrication of flexible graphene oxide paper-like adsorbent doped with magnetite nanoparticles for removal of dyes, *Res. Chem. Intermed.* (2021) 1–13.
- [66] E.P. Komarala, S. Nigam, M. Aslam, D. Bahadur, In-vitro evaluation of layered double hydroxide–Fe₃O₄ magnetic nanohybrids for thermo-chemotherapy, *New J. Chem.* 40 (2016) 423–433.
- [67] B. Lesiak, N. Rangam, P. Jiricek, I. Gordeev, J. Tóth, L. Kövér, M. Mohai, P. Borowicz, Surface study of Fe₃O₄ nanoparticles functionalized with biocompatible adsorbed molecules, *Front. Chem.* 7 (2019) 642.
- [68] L. Stobinski, B. Lesiak, A. Malolepszy, M. Mazurkiewicz, B. Mierzwa, J. Zemek, P. Jiricek, I. Bieloshapka, Graphene oxide and reduced graphene oxide studied by the XRD, TEM and electron spectroscopy methods, *J. Electron. Spectrosc. Relat. Phenom.* 195 (2014) 145–154.
- [69] N. Matinise, K. Kaviyarasu, N. Mongwaketsi, S. Khamlich, L. Kotsedi, N. Mayedwa, M. Maaza, Green synthesis of novel zinc iron oxide (ZnFe₂O₄) nanocomposite via moringa oleifera natural extract for electrochemical applications, *Appl. Surf. Sci.* 446 (2018) 66–73.
- [70] K. Kaviyarasu, C.M. Magdalane, D. Jayakumar, Y. Samson, A. Bashir, M. Maaza, D. Letsholathebe, A.H. Mahmoud, J. Kennedy, High performance of pyrochlore like Sm₂Ti₂O₇ heterojunction photocatalyst for efficient degradation of rhodamine-B dye with waste water under visible light irradiation, *J. King Saud. Univ. Sci.* 32 (2020) 1516–1522.
- [71] Y. Hou, J. Yu, S. Gao, Solvothermal reduction synthesis and characterization of superparamagnetic magnetite nanoparticles, *J. Mater. Chem. A* 13 (2003) 1983–1987.
- [72] K.J. Klabunde, R.M. Richards, *Nanoscale Materials in Chemistry*, John Wiley & Sons, 2009.
- [73] V.K. LaMer, R.H. Dinegar, Theory, production and mechanism of formation of monodispersed hydrosols, *J. Am. Chem. Soc.* 72 (1950) 4847–4854.
- [74] A.J. Barker, B. Cage, S. Russek, C.R. Stoldt, Ripening during magnetite nanoparticle synthesis: Resulting interfacial defects and magnetic properties, *J. Appl. Phys.* 98 (2005) 063528.
- [75] N.T. Thanh, N. Maclean, S. Mahiddine, Mechanisms of nucleation and growth of nanoparticles in solution, *Chem. Rev.* 114 (2014) 7610–7630.
- [76] S.G. Kwon, T. Hyeon, Colloidal chemical synthesis and formation kinetics of uniformly sized nanocrystals of metals, oxides, and chalcogenides, *Acc. Chem. Res.* 41 (2008) 1696–1709.
- [77] J.Y. Rempel, M.G. Bawendi, K.F. Jensen, Insights into the kinetics of semiconductor nanocrystal nucleation and growth, *J. Am. Chem. Soc.* 131 (2009) 4479–4489.
- [78] J. Polte, Fundamental growth principles of colloidal metal nanoparticles—a new perspective, *CrystEngComm* 17 (2015) 6809–6830.
- [79] A. Lassenberger, T. Grunewald, P. Van Oostrum, H. Renhoffer, H. Amenitsch, R. Zirbs, H. Lichtenegger, E. Reimhult, Monodisperse iron oxide nanoparticles by thermal decomposition: elucidating particle formation by second-resolved in situ small-angle X-ray scattering, *Chem. Mater.* 29 (2017) 4511–4522.
- [80] A. Zhu, P. Shi, S. Sun, M. Rui, Construction of rGO/Fe₃O₄/PANI nanocomposites and its corrosion resistance mechanism in waterborne acrylate-amino coating, *Prog. Org. Coat.* 133 (2019) 117–124.
- [81] A. Marikutsa, M. Rumyantseva, E.A. Konstantinova, A. Gaskov, The key role of active sites in the development of selective metal oxide sensor materials, *Sensors* 21 (2021) 2554.
- [82] A. Maleki, Z. Hajizadeh, H. Abbasi, Surface modification of graphene oxide by citric acid and its application as a heterogeneous nanocatalyst in organic condensation reaction, *Carbon Lett.* 27 (2018) 42–49.
- [83] J. Smit, H.P.J. Wijn, Ferrites; philips technical library: eindhoven, the netherlands, 1959.
- [84] M. Unni, A.M. Uhl, S. Savliwala, B.H. Savitzky, R. Dhavalikar, N. Garraud, D.P. Arnold, L.F. Kourkoutis, J.S. Andrew, C. Rinaldi, Thermal decomposition synthesis of iron oxide nanoparticles with diminished magnetic dead layer by controlled addition of oxygen, *ACS Nano* 11 (2017) 2284–2303.
- [85] L. Cabrera, S. Gutierrez, N. Menendez, M. Morales, P. Herrasti, Magnetite nanoparticles: electrochemical synthesis and characterization, *Electrochim. Acta* 53 (2008) 3436–3441.
- [86] Y. Wu, M. Fang, L. Lan, P. Zhang, K.V. Rao, Z. Bao, Rapid and direct magnetization of goethite ore roasted by biomass fuel, *Sep. Purif. Technol.* 94 (2012) 34–38.
- [87] S. Upadhyay, K. Parekh, B. Pandey, Influence of crystallite size on the magnetic properties of Fe₃O₄ nanoparticles, *J. Alloys Compd.* 678 (2016) 478–485.
- [88] J. Wallyn, N. Anton, T.F. Vandamme, Synthesis, principles, and properties of magnetite nanoparticles for in vivo imaging applications—A review, *Pharmaceutics* 11 (2019) 601.
- [89] R.A. Revia, M. Zhang, Magnetite nanoparticles for cancer diagnosis, treatment, and treatment monitoring: recent advances, *Mater. Today* 19 (2016) 157–168.
- [90] A.G. Kolhatkar, A.C. Jamison, D. Litvinov, R.C. Willson, T.R. Lee, Tuning the magnetic properties of nanoparticles, *Int. J. Mol. Sci.* 14 (2013) 15977–16009.
- [91] R.V. Chernozem, K.N. Romanyuk, I. Grubova, P.V. Chernozem, M.A. Surmeneva, Y.R. Mukhortova, M. Wilhelm, T. Ludwig, S. Mathur, A.L. Kholkin, Enhanced piezoresponse and surface electric potential of hybrid biodegradable polyhydroxybutyrate scaffolds functionalized with reduced graphene oxide for tissue engineering, *Nano Energy* 89 (2021) 106473.
- [92] S. Mishra, R. Sahoo, L. Unnikrishnan, A. Ramadoss, S. Mohanty, S.K. Nayak, Investigation of the electroactive phase content and dielectric behaviour of mechanically stretched PVDF-GO and PVDF-rGO composites, *Mater. Res. Bull.* 124 (2020) 110732.
- [93] T. Ludwig, M. Je, H. Choi, T. Fischer, S. Roitsch, R. Mueller, R.S. Mane, K.H. Kim, S. Mathur, Boosting nitrogen-doping and controlling interlayer spacing in pre-reduced graphene oxides, *Nano Energy* 78 (2020) 105286.
- [94] S.-H. Kang, T.-H. Fang, Z.-H. Hong, Electrical and mechanical properties of graphene oxide on flexible substrate, *J. Phys. Chem. Solids* 74 (2013) 1783–1793.
- [95] M. Pusty, L. Sinha, P.M. Shirage, A flexible self-poled piezoelectric nanogenerator based on a rGO-Ag/PVDF nanocomposite, *New J. Chem.* 43 (2019) 284–294.
- [96] M. Garle, J. Fentem, J. Fry, In vitro cytotoxicity tests for the prediction of acute toxicity in vivo, *Toxicol. Vitro* 8 (1994) 1303–1312.
- [97] K.G. Ozdemir, H. Yilmaz, S. Yilmaz, In vitro evaluation of cytotoxicity of soft lining materials on L929 cells by MTT assay, *J. Biomed. Mater. Res.* B 90 (2009) 82–86.

- [98] M. Daniyal, B. Liu, W. Wang, Comprehensive review on graphene oxide for use in drug delivery system, *Curr. Med. Chem.* 27 (2020) 3665–3685.
- [99] A. Farzin, S.A. Etesami, J. Quint, A. Memic, A. Tamayol, Magnetic nanoparticles in cancer therapy and diagnosis, *Adv. Healthc. Mater.* 9 (2020) 1901058.
- [100] M. Gasparotto, S. Pressi, A. Fortunato, G. Scapin, M. Mba, E. Menna, F. Filippini, Graphene-based scaffolds for regenerative medicine, *Nanomater.* 11 (2021) 404.
- [101] T. Pulingam, K.L. Thong, J.N. Appaturi, C.W. Lai, B.F. Leo, Mechanistic actions and contributing factors affecting the antibacterial property and cytotoxicity of graphene oxide, *Chemosphere* (2021) 130739.
- [102] A. Frtús, B. Smolková, M. Uzhychak, M. Lunova, M. Jirsa, Š. Kubinová, A. Dejneka, O. Lunov, Analyzing the mechanisms of iron oxide nanoparticles interactions with cells: A road from failure to success in clinical applications, *J. Control Release* (2020).
- [103] Y. He, C. Yi, X. Zhang, W. Zhao, D. Yu, Magnetic graphene oxide: synthesis approaches, physicochemical characteristics, and biomedical applications, *TrAC - Trends Anal. Chem.* (2021) 116191.
- [104] L.K. Di Wu, J. Tian, Y. Wu, J. Liu, Z. Li, X. Wu, Y. Huang, B. Gao, H. Wang, Z. Wu, Exosomes derived from bone mesenchymal stem cells with the stimulation of Fe₃O₄ nanoparticles and static magnetic field enhance wound healing through upregulated miR-21-5p, *Int. J. Nanomed.* 15 (2020) 7979.
- [105] M.A. Medina, G. Oza, A. Ángeles-Pascual, M. M. González, R. Antaño López, A. Vera, L. Leija, E. Reguera, L. Arriaga, J.M. Hernández Hernández, Synthesis, characterization and magnetic hyperthermia of monodispersed cobalt ferrite nanoparticles for cancer therapeutics, *Molecules* 25 (2020) 4428.
- [106] J. Park, S. Park, S. Ryu, S.H. Bhang, J. Kim, J.K. Yoon, Y.H. Park, S.P. Cho, S. Lee, B.H. Hong, Graphene - regulated cardiomyogenic differentiation process of mesenchymal stem cells by enhancing the expression of extracellular matrix proteins and cell signaling molecules, *Adv. Healthc. Mater.* 3 (2014) 176–181.
- [107] K.-H. Liao, Y.-S. Lin, C.W. Macosko, C.L. Haynes, Cytotoxicity of graphene oxide and graphene in human erythrocytes and skin fibroblasts, *ACS Appl. Mater. Interfaces* 3 (2011) 2607–2615.
- [108] Z. Guo, S. Kofink, H. Chen, J. Liang, D.W. Grijpma, A.A. Poot, Synthesis and characterization of rGO-graft-poly (trimethylene carbonate) for nerve regeneration conduits, *Biomed. Mater.* 14 (2019) 034101.
- [109] T.A. Salaheldin, S.A. Loutfy, M.A. Ramadan, T. Youssef, S.A. Mousa, Ir-enhanced photothermal therapeutic effect of graphene magnetite nanocomposite on human liver cancer HepG2 cell model, *Int. J. Nanomed.* 14 (2019) 4397.
- [110] P. Zan, C. Yang, H. Sun, L. Zhao, Z. Lv, Y. He, One-pot fabricating Fe₃O₄/graphene nanocomposite with excellent biocompatibility and non-toxicity as a negative MR contrast agent, *Colloids Surf. B* 145 (2016) 208–216.
- [111] W. Zhang, G. Yang, X. Wang, L. Jiang, F. Jiang, G. Li, Z. Zhang, X. Jiang, Magnetically controlled growth-factor-immobilized multilayer cell sheets for complex tissue regeneration, *Adv. Mater.* 29 (2017) 1703795.